The Hebrew University of Jerusalem האוניברסיטה העברית בירושלים

The Faculty of Mathematics and Sciences,

Edmond Safra (Givat Ram) Campus,

Institute of chemistry

Intense laser-field interaction with molecular anions

Deciphering the single and multi-detachment of SF_6^-

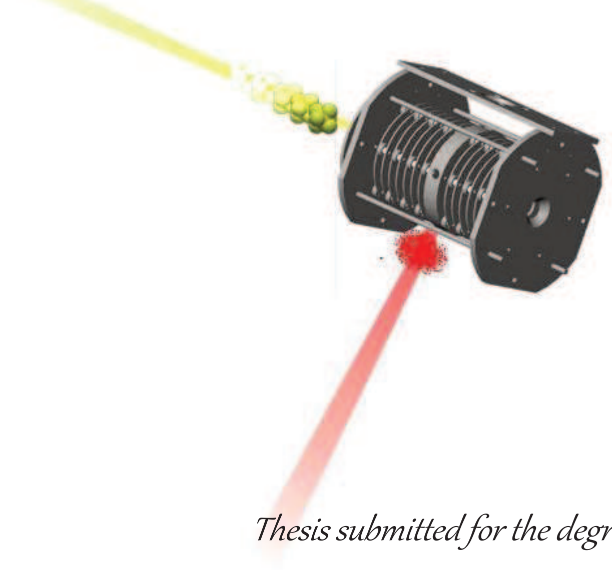

Thesis submitted for the degree of

"Master of Sciences"

in Physical Chemistry

Submitted by Yishai Albeck

ID: 02176112-7

Supervisor: Dr. Daniel Strasser

March 2013

Acknowledgements

This work is dedicated first and foremost to my parents, Amnon and Shira Albeck, who stimulated my curiosity and love of knowledge from childhood and throughout the years of my education leading to this research. Their un-biased advice on the one hand, and valuable academic experience on the other, have been priceless and I am immeasurably grateful to them for their help and encouragement in completing this research.

I wish to thank my adviser, Dr. Daniel Strasser for having the endless patience to enrich me with all the theoretical and experimental practice required for my academic research. I am especially thankful to him for letting me take part in his fascinating new lab, and for making my first years of research an endless spring of educational progress.

I would also like to thank my fellow student and friend, Avraham Klein, for numerous hours of learning, both religious and academic, which were sometimes overlapping, and both valuable and mentally encouraging.

Last but not least, I owe my gratitude to my wife, Naama, for supporting me in my decisions, and for managing and caring for our wonderful children throughout the long hours the research demanded from me, and for respecting my varied preoccupations.

"Wisdom and knowledge is granted unto thee" (Chronicles B 1,12)

Abstract

Interaction of intense laser pulses with finite systems of matter such as molecules or small clusters, exhibits rich phenomena that are sensitive not only to the laser wavelength, but also to the field intensity and temporal shape of the laser pulse. Studies on overall neutral and positively charged atoms and molecules have shown that at the intense field regime non-linear interactions become important as field intensity is increased and can be classified by the number of photons involved in the interaction. Eventually, as the electric field of light becomes comparable and even exceeds the forces that bind electrons to nuclei, the intense laser field can be considered as an oscillating electric field. In this regime, tunnel ionization is appreciable and phenomena such as electron recollision become significant, leading to observations of double ionization, high order harmonic generation, and coulomb explosion. On the other hand, there are only few works on the interactions of atomic anions with intense laser fields and no such studies performed on molecular anions. We present new experimental measurements of single and multiple photo-detachment of SF_6^- molecular anions by ultrafast and intense laser pulses aimed at understanding the role of the excess electron in these processes.

A dedicated fast ion beam photo-fragment spectrometer was constructed to allow mass selected preparation of SF_6^- anions and measurement of light matter interaction products. We find that the multiple-detachment dissociation is relatively isotropic and displays surprisingly weak dependence on the laser intensity and polarization ellipticity. Pulse shape dependencies are presented, in particular chirp and TOD that exhibit significant multiple detachment suppression by negative TOD. Weak dependence on laser ellipticity indicates non-significant role of recollision mechanisms that dominate interactions of neutral species with intense fields. However, the suppression by negative TOD pulses is interpreted to be due to premature removal of the weakly bound electron by the resulting pre-pulses, indicating the important role of the weakly bound electron in the detachment of additional electrons.

Table of Contents

1. Introduction

The invention of lasers revolutionized the study of light-matter interactions and photochemistry in particular. Laser spectroscopy is regularly used in a wide range of applications to identify molecular compositions at remote distances[1] and under the microscope[2,3,4,5,6]. The ongoing technological developments leading to shorter and shorter laser pulses allows ultra-short laser pulses to excite and to probe time resolved molecular reaction dynamics, resolving molecular vibrational and rotational motion with femto-second time resolution[7,8,9]. Temporal focusing of pulsed laser energy to femto-second time scales enables lasers to reach the intense field regime, in which the forces induced by the oscillating electric field of light are comparable and even exceed the intra-molecular forces[10]. In this regime new non-linear photochemical phenomena allow to further enhance our ability to manipulate both the laser light, which wavelength can be converted through non-linear interactions with matter[11], and non-linear photochemistry that can be controlled by subtle changes in laser pulse shapes[12,13,14].

Investigation of intense field photochemistry in overall neutral systems revealed a variety of non-linear phenomena, e.g. laser induced AC stark-shifts[15], bond softening[16,17], multi-photon ionization (MPI)[10,18], above threshold ionization (ATI)[18,17,19], Coulomb explosion[17,20,21] and more[22]. Measurements of intense field multiple ionization led to the development of the recollision mechanism[23] that successfully explained the surprising high order harmonic generation and double ionization of neutral species in the so called three step model. In this model, the simple picture of tunnel ionization by the intense field, followed by electron acceleration in the oscillating electric field, leading to recollision that can result in multiple ionization or high harmonic emission, paved the way for the recent achievements in atto-second pulse generation[24] and electronic wave-function tomography[25].

Although the majority of systems investigated with intense laser fields are overall neutral molecules[26,27], intense field photochemistry of molecular cations plays a crucial role in the evolving dynamics after the first electron is removed from a neutral system. Several dedicated experiments were performed to separately examine the photochemistry of carefully prepared isolated molecular cations[28,29,30]. On the other hand, one can expect that intense field interactions with molecular anions are significantly different from both neutral and cationic systems. Molecular anions are distinct in their comparatively weakly bound electron. Furthermore, as opposed to neutrals and cations, the first electron which is removed from an anion does not experience the long range Coulomb attraction of the ionized system.

Only few intense-field experiments were performed for anionic systems[31,32,33,34,35], primarily for atomic anions such as F^- and H^-. The photo-detachment processes were dominated by the sequential mechanism[32,34], though evidence of recollision was indicated by a couple of measurements[32], especially for heavier ions[35]. Molecular anions are expected to provide additional insight into the role of the weakly bound electron on multiple detachment mechanism. In addition to the effect of molecular complexity on multiple detachment of electrons, molecular systems are expected to exhibit rich dissociation dynamics leading to multiple final product channels. For example, multiply-ionized molecular systems can undergo Coulomb explosion or multiple electron dissociative ionization (MEDI)[36].

In this work we wish to extend earlier studies to include molecular anions interaction with intense laser fields. A new experimental setup with a dedicated photo-fragment spectrometer was designed, constructed and characterized. First experiments on the interaction of intense 800nm laser pulses with sulfur hexafluoride SF_6^- molecular anions are presented, aiming to provide a clearer picture of the role of the weakly bound electron.

In the following chapter the SF_6 system will be presented, followed by the background needed to discuss ultrafast intense laser pulses and selected non-linear processes. Chapter 3 outlines the objectives and motivation of this study, while Chapter 4 is devoted to a full description of our experimental setup, and the different measuring capabilities it allows. Since this is a very complex system, the establishment of the experimental setting is a major achievement of this work and therefore constitutes a major part of this study. Chapter 5 is dedicated to laser pulse characterization measurements, while results for the SF_6^- interaction with intense laser pulses are presented and discussed in chapter 6. We then summarize our results and conclude with proposals for future research.

2. Background

2.1. The molecular system

In the present work we explore the intense field interaction with the SF_6^- molecular anion. The properties of the neutral SF_6 system were extensively explored both experimentally and theoretically[37,38,39,40,41], as were the properties of its anionic derivative[42,43,44].

In addition to the basic research interest, sulfur hexafluoride gas is also used in several industrial applications, such as in the electrical industry[45], and as an etchant in the semiconductor industry[46]. This is due to some of its prominent properties, specifically chemical inertness and high dielectric strength. The stability of the neutral SF_6 system, combined with its inertness makes it a green-house gas with rising importance[47]. In fact, the extremely long lifetime of neutral SF_6 molecules in the earth atmosphere is limited only by their destruction in collisions with electrons, leading to the formation of anions and eventually SF_6 destruction. The work presented here on SF_6^- interaction with intense laser fields is part of a larger effort to improve our understanding of SF_6 destruction by electrons by developing time resolved probing of the dissociative dynamics of excited SF_6^- molecules.

Figure 2 shows some of the relevant potential curves of the neutral, anionic and cationic SF_6 systems and their respective energetics as a function of the S-F bond distance. The removal of an electron from the neutral SF_6 system destabilizes the system and leads to dissociative ionization with the SF_5^+ appearance energy measured[48] to be 15.3±0.2eV. On the other hand, addition of an excess electron to the SF_6 molecule leads to a stable molecule with 1.61±0.05eV dissociation energy[49] and a significant shift in the S-F bond length from 1.57 to 1.72Å[50]. One of the dramatic consequences of the bond length shift is the large difference between vertical electron detachment energy and the adiabatic detachment energy that are estimated to be 3.16[51,cf.50] and 1.03eV[52,cf.50] respectively. Following the debate[53,54] over the symmetry of SF_6^-, recent calculations[55] suggest that in addition to elongation of the

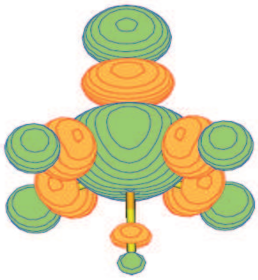

Figure 1: a-symmetric electronic density structure of SF_6^-, according to Eisfeld (ref. 55)

bond length, unequal distribution of the excess electron density leads to the breaking of the octahedral symmetry of neutral SF_6 molecule, which explained the unexpected peaks observed in high resolution photoelectron spectroscopy[43].

It is important to compare the SF_6 system energetic to the photon energy of 800nm laser pulses employed in our experiments. Photon energies of 1.03eV (1.2μm) can excite SF_6^- above its adiabatic detachment energy, making a single photon detachment mechanism energetically feasible. However, 1.55eV (800nm) photons fall in the large gap between the adiabatic and vertical detachment energies. Therefore, two photons or more are required for a vertical transition to occur from the SF_6^- ground state to a vibrational wavepacket on the neutral SF_6 potential. Furthermore, the energetic proximity of the SF_6^- dissociation energy is expected to produce rich dynamics of the competing product channels even for low laser fields.

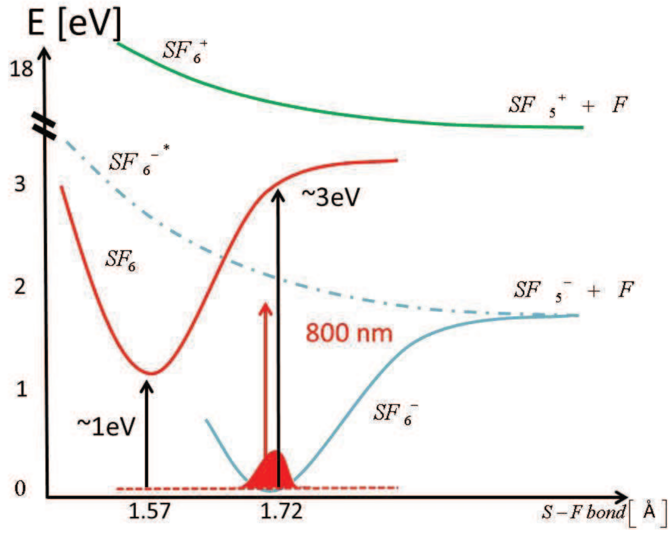

Figure 2: potential curves of the molecules participant in the photo-detachment reaction; SF_6^-, SF_6, SF_6^+. Illustrated by arrows are the channels of vertical and adiabatic excitation of the anion. Ionization energies and bond lengths are taken from recent literature (see text).

Table 1: appearance energies for the different SF_6^+ fragmentation products, measured by electron-ion coincidence measurements.

Ion	AE (eV)
F^+	38±1[a]
S^+	37±1 [a]
FS^+	31±1 [a]
F_2S^+	26±1 [a]
F_3S^+	19.4±0.5[b]
F_4S^+	19.1±0.5 [b]
F_5S^+	15.3±0.2 [b]

[a] A. Hitchcock, MVd. Wiel, J. Phys. B: Atom Molec. phys. 12, 1979

[b] M. Sasanuma et-al, J. Phys. B: Atom Molec. phys. 12, 1979

As mentioned in the introduction, intense fields can lead to the removal of multiple electrons and drive processes that are energetically not accessible with one or even two photon energies. **Table 1** shows a compilation of the appearance energies of the different cationic products of ionization[38,48]. As the SF_6^+ parent cation is inherently unstable, the first appearance energy of SF_5^+ cations lies at 15.3±0.2eV that is the equivalent to 10 photons. Higher fragmentation levels, forming atomic S^+ and F^+ products indicate a complete dissociation of the SF_6 system and begin to appear at energies above 37eV. Energetically, 24 or more 800nm photons are required to reach these multiple dissociative detachment thresholds from the anion ground state. One of the aims of this work was to explore the possibility that, similar to multiple-ionization of many neutral systems, such highly excited products may be produced by a recollision mechanism.

Early experiments with the neutral molecule which indicated that double detachment of SF_6 leads to dissociation (DDI), showed that surprisingly the fragmentation pattern was constant throughout a range of impact energies, in spite of resonant levels that might have affected the active fragmentation channels[56]. The probabilities of the different channels were deduced from TOF spectrums[38], and the contribution from DDI was verified, including F^+ that was formally thought[37] to have evolved as an ion pair with F^-. Coulomb explosion products were measured, the kinetic energy evidently transferred only to the fluorine atoms, but no indication to recollision was stated.

2.2. Intense lasers

As mentioned in the introduction, the development of lasers that produce ultrashort pulses of light allows exploring the interaction of intense fields that peak during the laser pulse. While continuous wave (CW) lasers can produce a well-defined narrow wavelength, pulsed lasers require a minimal bandwidth that is inversely related to the duration of the pulse. It is comfortable to approximate the spectral content with a Gaussian spectrum, defined by a center frequency ω_0 and a 1/e bandwidth σ_ω, due to the Fourier relation between the frequency and time domains:

(1) $$E(\omega) = E(\omega_0)e^{-\frac{(\omega-\omega_0)^2}{\sigma_\omega{}^2}}$$

$$E(t) \ = \frac{1}{\sqrt{2\pi}}\int_{-\infty}^{\infty} E(\omega)e^{i\omega t}dt$$

$$= E(t_0)e^{-\frac{(t-t_0)^2}{\sigma_t{}^2}}$$

In this approximation the bandwidth can be related to the minimal length of the pulse in time through the uncertainty relation in **equation 2**:

(2) $$\sigma_\omega \sigma_t = 1$$

Where the 1/e field width, σ, is related to the practical FWHM bandwidth or temporal width of the intensity profile through $\Delta_{FWHM} = \sqrt{2\ln 2}\sigma$.

A deviation from a transform limited time profile will be seen when the phase of the electric field depends on wavelength. **Equation 3** shows an expansion of the spectral phase around the central frequency of the pulse.

(3) $$\varphi(\omega) = \varphi_0 + \varphi_1(\omega - \omega_0) + \varphi_2(\omega - \omega_0)^2 + \varphi_3(\omega - \omega_0)^3 + \cdots$$

The first term (φ_0) is the Carrier Envelope Phase (CEP), as it determines the phase of the electric field in regards to the pulse envelope. The linear term, φ_1, can be shown to be a time shift of the pulse:

(4) $$E(t) = \frac{1}{\sqrt{2\pi}}\int_{-\infty}^{\infty} E(\omega)e^{i\left(\omega t - \varphi_1(\omega-\omega_0)\right)}dt$$

$$= \frac{1}{\sqrt{2\pi}}\int_{-\infty}^{\infty} E(\omega)e^{i(\omega(t-\varphi_1)+\varphi_1\omega_0)}dt$$

$$= \frac{1}{\sqrt{2\pi}}\int_{-\infty}^{\infty} E(\omega)e^{i(\omega(t-t_1)+\tilde{\varphi}_0)}dt$$

In the same way, the quadratic term is the frequency chirp as a function of time that effectively changes the temporal width of the pulse:

(5) $$E(t) = \frac{1}{\sqrt{2\pi}}\int_{-\infty}^{\infty} E(\omega)e^{i\left(\omega t - \varphi_2(\omega-\omega_0)^2\right)}dt$$

$$= \frac{1}{\sqrt{2\pi}}\int_{-\infty}^{\infty} E(\omega)e^{i\left(\omega\left(t-t_2(\omega)\right)+\tilde{\tilde{\varphi}}_0\right)}dt$$

One side of the frequencies relative to ω_0 will be shifted to later times and the other to earlier times, increasing the width. The convention is tailing high frequencies for positive chirp.

The next term (Third Order Dispersion – TOD) results in an a-symmetric time profile also subject to interference. **Figure 3**[57] illustrates the effect of the different terms in both temporal profile and in Wigner representation, showing time and frequency dependencies together.

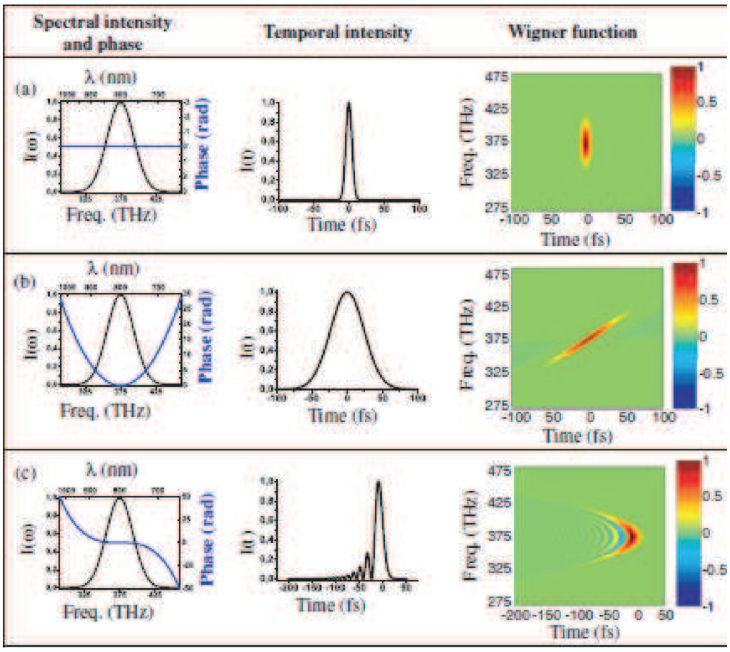

Figure 3: illustrations of spectral and temporal profiles of a non-distorted pulse (a), and the effect of adding chirp (b) and TOD (c). On the right is presented the Wigner representation of the spectrum displaying both domains. This is useful for understanding the temporal role of the different frequencies in the pulse.

The temporal length of a pulse corresponds to the time required for a defined fraction of the pulse (either intensity FWHM or by other definitions such as the field 1/e decay defined above) to pass through a plane perpendicular to its propagation axis. Up-to-date intense lasers reach pulse lengths of down to few femto-seconds and even less, and distortions in the phase bring forth to elongation of the pulse length. For a Gaussian pulse, pulse elongation due to chirp can be expressed analytically through:

(6) $\Delta_t(\varphi_2) = \Delta_t(0)\sqrt{1 + (4ln2\frac{\varphi_2}{\Delta_t(0)^2})^2}$

Laser pulses with short temporal widths reach high peak intensities, the intensity profile related to the electric field through:

(7) $I(t) = \frac{1}{2}c\varepsilon_0 n|E(t)|^2$

This relation makes use of the physical properties c, ε_0 and n representing the light velocity, vacuum permittivity and index refraction respectively.

For a Gaussian laser beam with optical power P_{laser}, **equation 8** indicates that a few Watt may be enough for achieving high intensities by focusing all the energy constricted within the laser beam, U_{laser}, both spatially to an area A_{beam}, and temporally to Δ_t. Using pulsed lasers in the order of femto-second temporal widths, and spatially focusing the laser via optical lens to beam waists of a few micro-meters, intensities on the order of 10^{16} W/cm^2 are achieved:

(8) $$\begin{aligned} I_{laser} &= \frac{2P_{laser}}{A_{beam}} \\ &= \frac{2U_{laser}}{A_{beam}\Delta_t} \\ &= \frac{2 \cdot 3mJ}{\pi(14\mu m)^2 25fs} \\ &\cong 4 \cdot 10^{16}\frac{W}{cm^2} \end{aligned}$$

The consequence of these high intensities on laser-matter interactions lies in the prospect of non-linear processes.

2.3. Non-linear ionization

The non-linearity of the processes we investigate refers to the dependence of the process on the intensity of the laser. Albert Einstein in his famous, Nobel awarded, photo-electric-effect paper[58] introduced quantization of light to explain how the threshold frequency of light required to extract electrons from matter is not affected by the intensity of a light source. This observation is strictly true only for weak light fields, in which interactions with matter are dominated by linear, single photon processes. With increasing field intensities, non-linear processes can allow extracting electrons from matter even if the required ionization energy is higher than the energy of a single quantum of light. The typical ionization energies of 10eV and more, required for extracting bound electrons from molecular systems, are significantly higher than the photon energies at visible wavelengths. Nevertheless, high enough intensities lead to significant multi-photon ionization (MPI)[10,18]. The absorption of multiple photons in a short period of time before the system can release the absorbed energy strongly depends on the photon density or in other words peak intensity. Such ionization can be dramatically enhanced by the presence of favorable resonances, a phenomenon that can lead to selective ionization of specific species and is known as resonance enhanced multi-photon ionization (REMPI)[59]. The high intensities which are accessible with ultrafast lasers may even lead to ionization of a molecule with more than the required number of photons, known as above threshold ionization (ATI)[60].

The description of an intense field interaction by considering multiple steps of resonant and non-resonant photo-absorption is highly useful as long as the interaction with the laser field can be treated perturbatively. Reaching yet higher intensities, with corresponding fields comparable and even exceeding the forces binding the electrons to the nuclei, it is more appropriate to consider the light as an oscillating electric field induced on the chemical system. **Figure 4** illustrates how the time dependent ionization rate can be evaluated by the rate of tunneling through the combined potential of an atom and the potential induced by the instantaneous electric field, $E(t)$. The ionization rate ω_{tunn} at the electric field, E_0, can be expressed by **equation 9**, where IP is the ionization potential and m_e and e are the electron mass and charge respectively (full derivation and details in Appendix A).

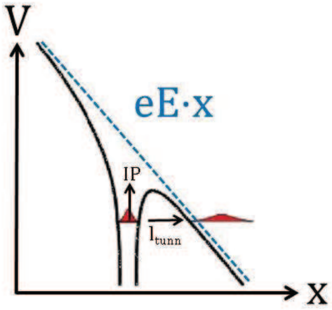

Figure 4: illustration of an electron tunneling in the presence of a strong electric field.

(9) $$\omega_{tunn} = eE_0\sqrt{\frac{2}{IP\cdot m_e}}$$

In contrast to the multi-photon description, in which the optical oscillation frequency plays a crucial role, in the tunnel ionization description ionization can occur within a single half cycle of light. It is therefore useful to define the Keldysh parameter[61], γ, which is defined as the ratio of twice the optical frequency, ω_0, and the peak tunneling rate.

(10) $$\gamma = \frac{2\pi c}{e\lambda}\sqrt{c\varepsilon_0 n m_e}\cdot\sqrt{\frac{IP}{I_0}}; \qquad \gamma \equiv \frac{2\omega_0}{\omega_{tunn}}$$

Where I_0 is the peak intensity in W/cm^2, λ is the wavelength in nm and the other signs are defined in **equations (7)** and **(9)**.

A high tunneling rate would imply to the occurrence of significant tunneling, defined by a very small Keldysh parameter satisfying $\gamma \ll 1$. We can quantify the required intensities for electron tunneling for a few processes regarding SF_6^-, substituting IP with the relevant energies, summarized in **table 2**:

	Energy	Intensity (satisfying $\gamma = 1$)
Adiabatic detachment of SF_6^-	$\sim 1eV$	$0.08 \cdot 10^{14} W/cm^2$
Vertical detachment of SF_6^-	$\sim 3eV$	$0.25 \cdot 10^{14} W/cm^2$
Appearance of SF_5^+	$\sim 15eV$	$1.26 \cdot 10^{14} W/cm^2$
Appearance of SF_6^{2+}	$\sim 39eV$ [62,63]	$3.27 \cdot 10^{14} W/cm^2$

Table 2: intensities at the turning point from MP detachment to the tunneling regime, for some photo-detachment processes regarding SF_6^-

As indicated above, intensities on this scale and higher are made possible by ultrafast lasers, which enable the non-linear processes we explore, specifically the double and multiple detachment of electrons. The double ionization process was observed for a variety of molecules and atoms[64,65,66], and in itself is usually assigned one of two mechanisms. The first is said to be sequential, referring to a second occasion of either MPI or TI occurring to a second electron in a later part of the pulse. On the other hand, a non-sequential (NS) process relates to the case when both electron detachments emerge from a single event. While the sequential description is easily understood, regarding its mechanism, the NS case requires extended understanding as to the exact mechanism responsible for its execution.

Studies performed first on atomic Kr[67] and later also on other systems[68] showed that double ionization occurs at much lower intensities than could be explained by sequential tunnel ionization of the two electrons. Furthermore, it was found that interaction of intense laser pulses with atoms and molecules in the gas phase can generate unexpected high order odd harmonics of the fundamental laser frequency (HHG), with up to keV photon energies[69]. A successful semi-classical explanation for these two phenomena was first given in 1993 by Paul Corkum[23]. In the so called "three step model", depicted in **figure 5**, the first step is indeed governed by the Keldysh parameter and tunnel ionization of the less bound electron. In the next step the now free electron is accelerated in the oscillating electric field of light, thus accumulating high kinetic energy that can reach $3.17U_p$, where U_p is the pondermotive potential which is equal to $U_p = \frac{e^2E^2}{4m_e{\omega_0}^2}$. In the third and last step, the electron, which is driven back into the system, can cause double ionization by releasing another electron in the collision. Alternatively, it can radiatively recombine with the system and emit its excess energy as a high energy HHG photon. As this process coherently occurs twice in every cycle of the fundamental laser field, only odd harmonics of the fundamental frequency interfere constructively to form the observed odd harmonic spectrum.

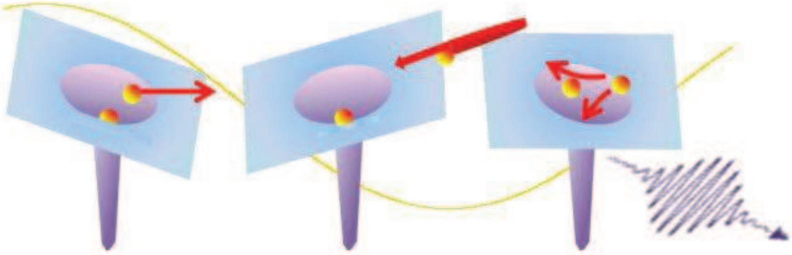

Figure 5: illustration of the three step model as proposed by Corkum along with the interacting laser field, which brings forth the single detachment, later accelerating it back to recollide with the parent molecule leading to double-detachment or radiative emission.

The three step model also explains the sensitivity of both double ionization and HHG to the ellipticity of the laser polarization – as even a small deviation from linear polarization will divert the trajectory of tunnel-ionized electron away from their source and suppress any processes related to its recollision with the parent molecule[70] (**figure 6**). Experimental observations of strong dependence of double ionization yields on the laser beam polarity[71], along with ion-momentum distribution measurements[72] which are distinct for recollision[66], provided evidence to the recollision mechanism, favoring it over previously proposed models[73]. The recollision model was further developed into second generation models to include detailed effects of the mechanism, and to deal with some of the discrepancies of the results[74].

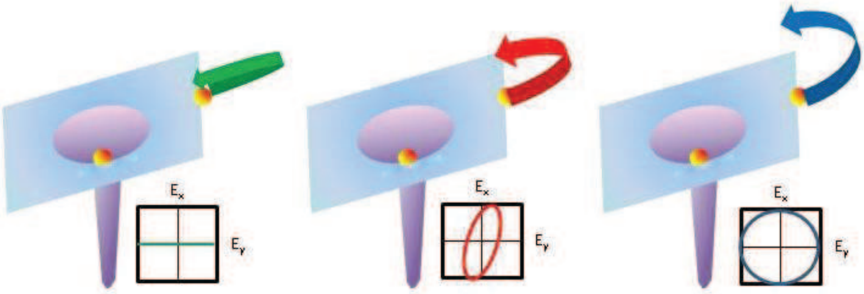

Figure 6: controlling the recollision yield by changing the ellipticity of the laser polarization.

Multiple detachments of two or more electrons not from an isolated atom, but from a molecular system, produces highly charged cations that are inherently destabilized as a result of the strong coulomb repulsion of the nuclei. Instantaneous removal of sufficient electrons from any molecular system will result in dissociation on the repulsive Coulomb potential. The so called Coulomb explosion leads to high kinetic energy release (KER) that can be related to the distances of nuclei in the molecular system. In the simple case of a diatomic molecule, exploding into two singly charged fragments, KER can be shown[75] to correspond to a simple relation:

(11) $$KER = \frac{14.4\ eV/A}{R_{bond}}$$

Coulomb explosion imaging, performed by stripping electrons from a fast moving molecule as it passes through a thin foil, was used for retrieving structural information even for polyatomic molecules[76]. However, intense field Coulomb explosion is dominated by the non-trivial interaction of intense fields with matter and is still the subject of extensive research, making the extraction of structural information very complicated even for molecules as simple as H_2[77].

3. Objectives and motivation

In our work we extend the field of non-linear light-matter interactions to molecular anions. These systems, populated by an excess electron, have ionization potentials different from the typical high IPs of neutral systems. The IP has an important role in the electron detachment process, and the process mechanism is often determined by it. Double detachment, too, may differ in character as the molecule relieved of the first electron is neutral, un-affecting this electron once liberated or when recolliding.

The choice of the SF_6^- molecule was elaborated above. In short it is an extensively investigated molecule, but its anionic form, like molecular anions in general, still remains unresolved in the context of the interactions we investigate.

We set out to resolve and understand more thoroughly the photo-detachment processes concerning SF_6^-, both single and multi-electron detachments. We wish to elucidate the relevant mechanisms as much as our measuring methodologies allow. Thus, our direct goal is to bring to perfection these methods, building a detailed scheme for these types of measurements, and to map the different possibilities corresponding to our results.

4. Experimental setup

Our experimental system combines two types of techniques: (I) A commercial ultrafast amplified Laser system[78,79] and (II) a home built fast ion beam fragment imaging apparatus. The setup allows exploring the interactions of mass selected molecular anions with ultrafast and intense laser pulses by detecting and resolving all the possible charged and neutral products of the photochemical reaction. **Figure 5** shows a schematic representation of the different parts of the experimental setup. Briefly, molecular ions of interest are generated by a pulsed supersonic expansion Even-Lavie ion source[80] located in vacuum chamber I. In chamber II, anions are accelerated in the direction of the laser-ion interaction region by electric fields induced by a set of pulsed electrodes, for time separating the ions based on their charge over mass ratio. The ion bunch can be further spatially focused, if needed, by an einzel lens positioned 315mm later. In chamber III, ions are mass selected based on their time of flight by a "mass gate" at the entrance of the photo-fragment spectrometer that deflects ions arriving at undesired times. Selected ions are collimated and accelerated by the electrodes of the spectrometer through the interaction region, in which the ion beam trajectory is crossed by the path of an amplified ultrafast laser beam. On their way out of the spectrometer, parent anions are decelerated and continue their way to a time and position sensitive MCP detector with their original velocities, while Laser-ion interaction products are separated during their flight towards the detector based on their charge and mass.

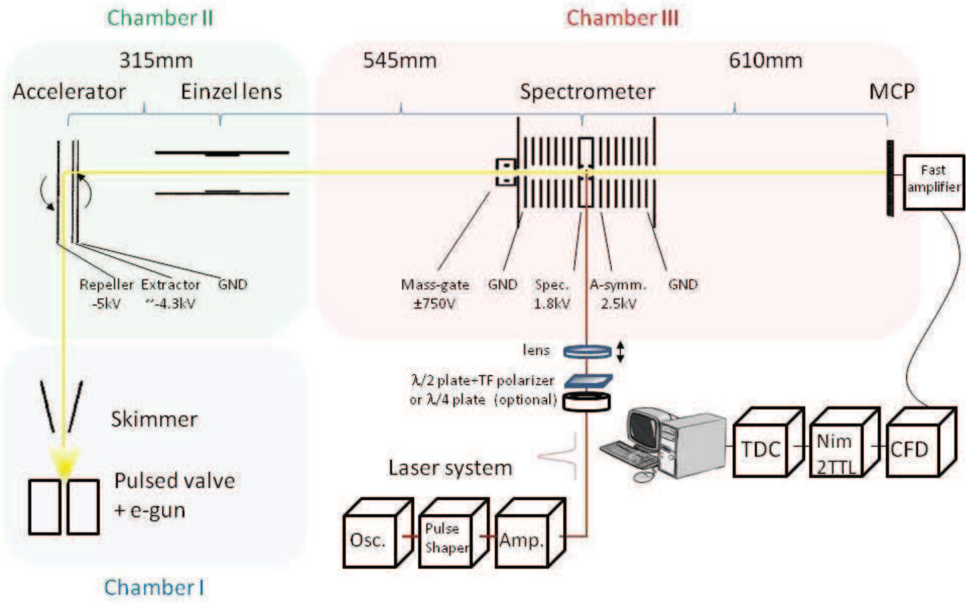

Figure 5: experimental setup. A combination of a high vacuum system, an intense fs laser system and a data acquisition set.

In the following I will describe in detail the different parts of the experimental setup.

4.1. The vacuum system

The vacuum system is divided into 3 differentially pumped vacuum chambers. Chamber I is pumped by a pair of 450L/s turbo molecular pumps, achieving a $4\cdot10^{-8}$ Torr background pressure and an average $4\cdot10^{-6}$ Torr pressure during typical operation of the experiment at a 333.3 Hz repetition rate, as measured in a cold cathode penning ionization pressure gauge. Chamber II is separated from chamber I by a 10mm diameter skimmer and is pumped by a 250 L/S turbo molecular pump. Chamber II background pressure, as measured by an ion gauge, reaches $6\cdot10^{-8}$ Torr, while an average $4\cdot10^{-7}$ pressure is measured during typical pulsed valve operation. Chamber III is separated from chamber II by a 38mm diameter and 425mm long tube and is pumped by a 125L/s turbo pump, reaching background and operation pressures of $4\cdot10^{-9}$ Torr and $2\cdot10^{-8}$ Torr respectively, as measured by another ion gauge. All the turbo molecular pumps are backed by a rotary vane pump, maintaining a backing pressure of about $4\cdot10^{-3}$ Torr during source operation.

Maintaining low pressures is significant, especially in the interaction chamber, to sufficiently decrease the background noise. This noise is mainly originated from water and hydrogen molecules sticking to the walls of the vacuum chambers. It can be considerably removed by baking of the system, literally heating the steal construction with electrical heating strips, thus getting to the low pressures mentioned.

This is extremely important for the analysis of our experiments since these residual gas molecules arrive at the detector at the same time as expected from our interaction products. Our analysis is based on the recording of the times at which particles hit the detector. These Times of Flight (TOF) refer to the time taken for the particle to reach the detector from an initial reference time. This, of course, requires the synchronization of the different devices, controlling the particles flight, and also the synchronization to the laser system, as described later in this chapter.

4.1.1. Ion source

Ions are generated using an Even-Lavie supersonic expansion ion source[80] that uses a pulsed electron gun for ionization. The Even-Lavie pulsed valve releases into the vacuum an 8 microsecond pulse of high pressure gas mixture, typically we use 200psi argon carrier gas seeded with a 1% SF_6 gas sample. Electrons are generated by a circular hot filament and a timed repelling high voltage pulse accelerates them through a grounded grid into the expanding gas pulse. Molecular anions, cations as well as neutral excited states are formed both due to direct interaction of fast electrons with the sample molecules as well as due to indirect interaction through metastable carrier gas states and slow secondary electrons. Due to multiple collisions with the rapidly expanding carrier gas, ions are cooled to temperatures as low as 10K and lower[81] and thus complexes and clusters that are unstable at room temperature can be formed. At sufficiently low temperatures (a few tens of K) that are reached by optimizing electron-gun and gas-expansion conditions, SF_6^- ions can even bind to argon atoms and clusters[43] as shown in **figure 6**.

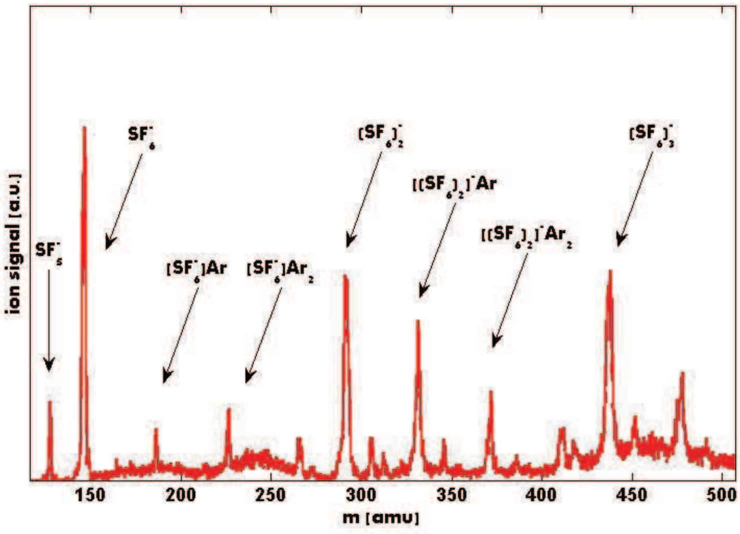

Figure 6: TOF spectrum of different anion cluster species. The times are calibrated and translated into mass. Besides the different cluster sizes, argon tagged anions are also formed, due to the low temperatures achieved during the ultrasonic expansion. We also get a molecule from which a fluorine atom was detached.

4.1.2. Ion acceleration and TOF-MS

Ions that are formed in the supersonic expansion ion source continue to fly in the speed of sound through a 10mm skimmer, separating chamber I and chamber II. At a time delay of ~$250\mu s$, ions reach the area between a pair of repeller and extractor electrodes that are kept grounded until a timed high voltage pulse accelerates the ions towards the interaction region with the laser. The potentials applied to the repeller and extractor electrodes (typically 5kV and ~4.3kV respectively) allow to independently tune the average energy of the resulting ion beam and to achieve time focusing of the ion bunch at the final detector or at the laser-ion interaction region in a Wiley-McLaren (W.M.) scheme[82] shown in **figure 7**. In this scheme the voltage drop between the repeller and extractor can be tuned to provide higher kinetic energy to ions that are closer to the repeller and further from the detector. This facilitates time focusing the ions, such that all the ions that are between the two electrodes reach simultaneously to the desired distance D. The higher the voltage difference, the greater the outer ions in the bunch are accelerated or decelerated in respect to the middle ones, and the bunch is focused earlier in flight.

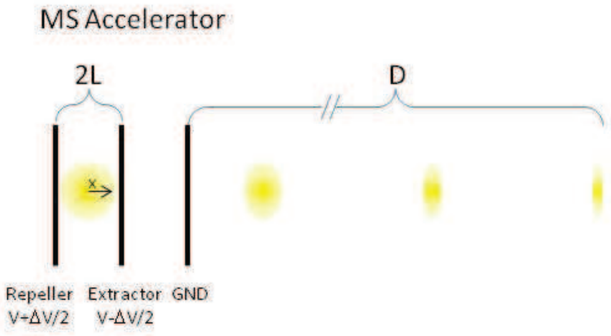

Figure 7: Whiley-McLaren scheme of accelerating electrodes, temporally focusing an ion beam at a distance D.

We can understand the W.M. time focusing conditions by dividing the accelerated ion flight into three time regions. The first refers to the time spent during acceleration between the repeller and extractor electrodes, and is described by **equation 12**:

$$t_{acc.} = \sqrt{\frac{4L(L-x)m}{q\Delta V}} \qquad (12)$$

Following **figure 7**, the ions initial position is defined by L and x, ΔV is the voltage drop between the repeller and the extractor that enables the focusing of the ion bunch, and q and m are the ions charge and mass respectively.

Due to the short time the ions spend in the second part of the accelerating region, and because of the small dependence of that time on x, we neglect this time and proceed with the third time after exiting the accelerating electrodes. The final velocity is determined by V, the potential at $x = 0$ between the repeller and extractor, and the time of the free flight until focusing at a distance D is described by **equation 13**:

$$\textbf{(13)} \qquad \boldsymbol{t_{free} = \frac{D}{\sqrt{2e(V - \frac{\Delta V}{2} \cdot \frac{x}{L})/m}}}$$

W.M. conditions for focusing at the distance D from the accelerating electrodes are reached by adjusting the potentials such that the first derivative of the TOF with respect to the initial position vanishes. **Equation 14** describes the relation between the controlled voltages that satisfy this condition, assuming $D >> L$ and approximating the total $\boldsymbol{TOF = t_{acc.} + t_{free}}$. One can easily see that in this first level approximation, W.M. conditions are independent of the ions mass.

$$\textbf{(14)} \qquad \boldsymbol{\frac{\partial TOF}{\partial x}|_{x=0} = \frac{\partial(t_{accelerated} + t_{free})}{\partial x}|_{x=0} = 0}$$

$$\rightarrow \quad \boldsymbol{(\frac{\Delta V}{V})^{3/2} = \frac{4\sqrt{2}L}{D}}$$

The focusing of the identical species may be crucial for distinguishing between different products, and for providing large enough densities of molecules for effectively measuring the interaction with the laser.

Two important regions of interest in the context of temporal focusing of the ion beam are at the interaction zone and at the detector. Focusing at the detector is important for identification of the different species measured as they are distinguished by their time of flight. Practically, optimizing the focusing at the detector is achieved by optimizing the extractor voltage to produce narrow peaks in the measured ion TOF spectrum and allow optimal mass resolution. Ions with a distribution of energies, and therefore accelerations, may still arrive simultaneously at the detector if W.M. conditions are reached, resulting with a narrow distribution of TOFs, and narrow peaks. **Figure 8** shows the process of focusing the anions temporally at the detector by tuning the extractor voltage.

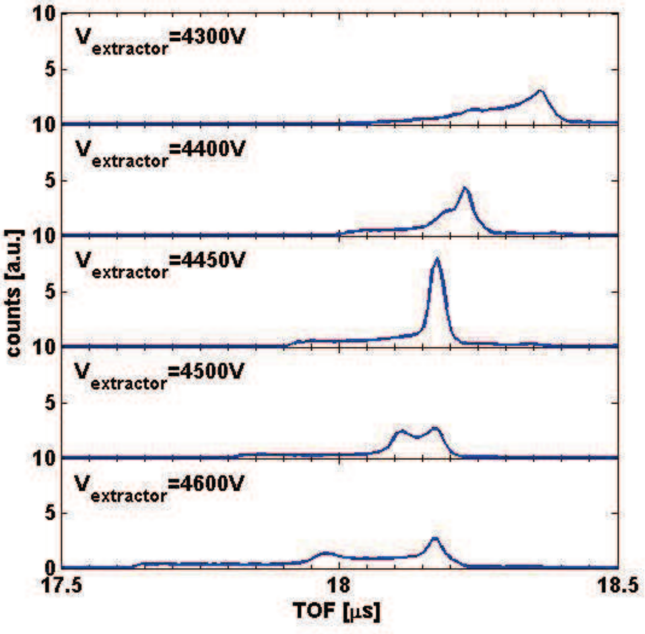

Figure 8: anion peaks as recorded on the detector for different extractor voltages. Optimal temporal focusing of the ions at the detector is observed with extractor voltage of 4.45kV by the narrow peak.

The second region of interest is in the middle of the photo-fragment spectrometer, where the interaction with the laser takes place. The focusing of the ion beam in this region optimizes the overlap of the ion bunch with the laser beam, enabling easier identification of the interaction products, and greater resolution with a better signal to noise ratio. Time focusing at the spectrometer also enhances the mass resolution of the mass-gate, located at the entrance of the photo-fragment spectrometer (see **figure 11**). As shown in **figure 9**, ion time focusing in the center of the spectrometer is measured by plotting the yield of neutral photo-detachment products as a function of the timing of the focused laser pulse, and its synchronization to the ions propagation in the interaction zone. A scan in which this timing is tuned, resolves the time the ion beam passes in the zone, namely its temporal focusing. It should be noted that the profile width of the scan actually expresses the convolution between the width of the two beams in the axis of ion flight, but as the few micro-meter wide laser beam is negligible in respect to the cm long ion bunch it can be treated as the ion's temporal width itself. This scan was re-measured for different extractor voltages, to find the optimal conditions for focusing the ion bunch in the interaction zone.

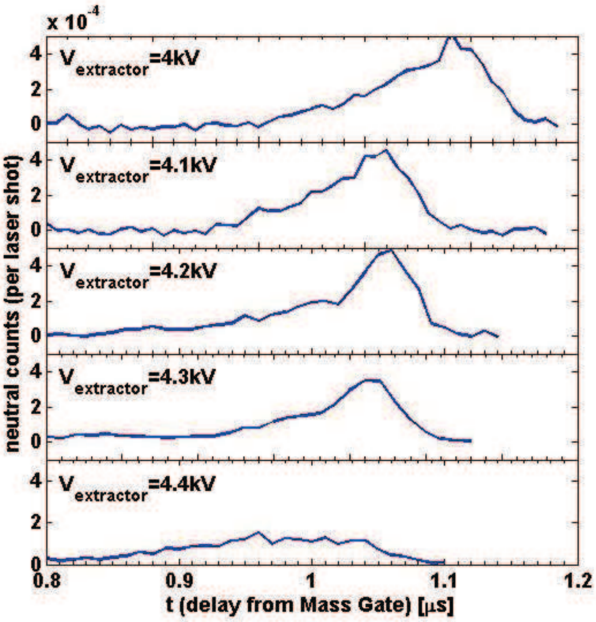

Figure 9: laser delay scans of neutral SF_6 yield, for different extractor voltages. Each scan reflects the ion bunch focusing in the axis of flight in the region of interaction. The a-symmetry between the profile before and after the focusing voltage reflects the a-symmetry of the ion bunch itself.

Detailed SIMION[83] ion trajectory simulations were carried out, including the actual experimental geometry and random initial conditions. Simulation results for time focusing at the detector and at the interaction zone are shown in **figure 10**. Considering the experimental deviation from simulation (due to slight geometrical and voltage discrepancies), an extractor voltage of about 4300V is optimal for the experiment, taking in consideration conditions in both regions.

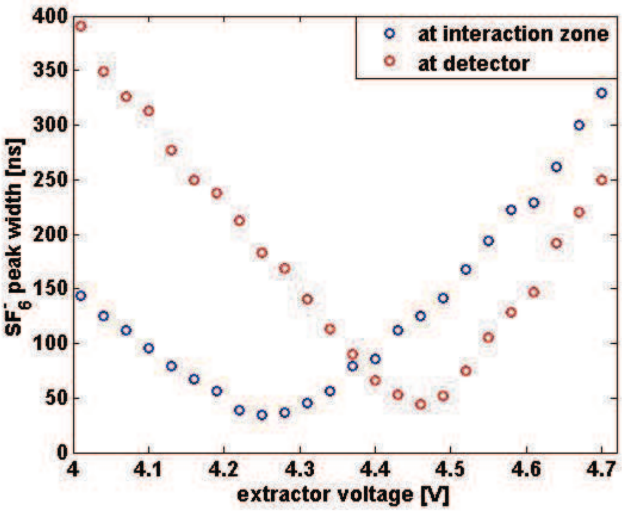

Figure 10: SIMION simulations for temporal width of ion beam, at both regions; interaction zone (blue) and detector (red), while tuning the extractor voltage, simulating the efficiency of the Wiley-McLaren focusing at both regions.

4.1.3. Photo-fragment spectrometer

The ion beam path leads it to our home-made photo-fragment spectrometer located in chamber III, the design of which is shown in **figure 11**. At the entrance side of the spectrometer, pulsed high voltages are applied to vertical deflector plates that act as a temporal mass gate (MG). The high voltages are grounded in a short time window that is timed to deflect all unwanted masses, while letting selected masses through. Ions that pass through the mass gate are accelerated by a series of equally spaced electrodes #1 - #8 supplied with uniformly rising potentials that ensure a uniform acceleration field for the parent molecular anions. The apertures in electrode #8 mechanically define the ion-laser interaction region, ensuring that a laser optical path passing through the vertical apertures intersect the ion beam path at the field free region in the middle of electrode #8. Potentials supplied to electrodes #10 - #15 are designed to provide a uniform deceleration of parent ions, while electrode #9 is supplied with a voltage which breaks the potential symmetry across the device, and prevents ions formed in the interaction of the intense laser with residual gas molecules from being accelerated towards the detector.

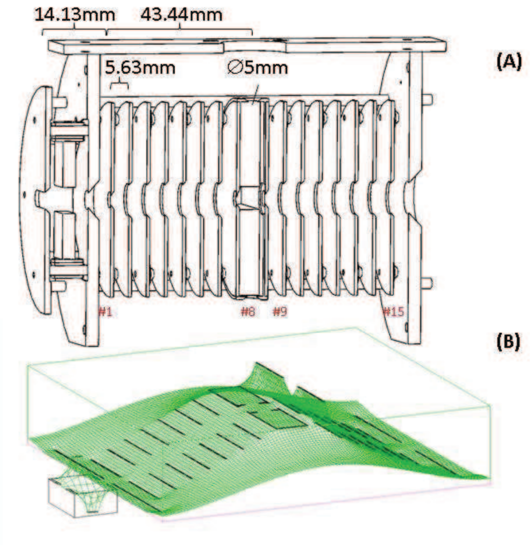

Figure 11: (A) section cut of Solid-Works drawing of our home-built spectrometer device. On the left the MG electrodes are apparent, as are the 14 electrodes surrounding the interaction zone electrode (applied voltages of 0-1.8kV), enabling mass-over-charge spectrometry.

(B) SIMION calculation of spectrometer potential surface. Positive potential accelerates the incoming anions, while in the down-hill it accelerates the cations (while the RG is blocked by the potential barrier).

The voltage applied in our setup (divided uniformly between the electrodes) was experimentally set to 1.8kV. This energy was found to be sufficient for the smallest component of the SF_6^+ fragmentation, positively charged fluorine atoms, to be left with enough energy to be detected by the detector.

An additional controlled electrode mentioned above breaks the symmetric potential setup which is supposed to prevent the acceleration of the residual gas present in the chamber, mainly composed of water and hydrogen molecules (Appendix B describes the contents in more detail). These molecules are also subjected to the intense laser, and are also ionized with some efficiency. Electric fields leaking into the almost field free interaction zone may accelerate ionized residual gas molecules, producing most of the background noise measured in these experiments. The residual gas TOF spectrum is placed in the time region of the SF_6 products, emphasizing the importance of reducing this noise. Appointing the additional voltage we create a barrier which indeed breaks the symmetry of the device, but also blocks the slow cations, originated by the residual gas which did not accumulate enough speed to pass this barrier. On the other hand, the SF_6^- molecules who were accelerated first by 5kV and then also by an additional 1.8kV in the first part of the spectrometer, fly at a speed of about $50\text{km}\cdot\text{sec}^{-1}$, enough to pass the barrier unaffected. Even the small fluorine cations left with a small fragment of this energy can pass a barrier of 2.5kV efficiently, while the residual gas is sufficiently suppressed. Appendix C describes in detail the choice of 1.8kV for the spectrometer voltage, and the corresponding 2.5kV a-symmetric voltage.

Neutral products of the single detachment, exit the interaction zone and fly at a constant velocity as they are unaffected by the second series of electrodes. In this way, they arrive at an earlier TOF than the parent anions. Further electron detachments produce cations that are accelerated on their way out of the spectrometer, arriving even earlier than the neutral products according to their charge over mass ratio.

Figure 12 demonstrates the operation of the mass selection and photo-fragment spectrometer, measuring the neutral photo-detachment products of water cluster anions. **Figure 12(A)** shows the TOF spectrum of water anion clusters $(H_2O)_n^-$, with ion source conditions optimized for n=11-21 and grounded MG electrodes. **Figure 12(B)** shows the mass gated TOF spectrum with only $(H_2O)_{15}^-$ anions arriving at the detector, selected by a mass gate time window of $1\mu s$ timed $10\mu s$ after the ion-bunch accelerating pulse. In order to synchronize arrival of the laser and ion pulses to the interaction region, we provide a $\sim 1\mu s$ time delay of the laser pulse with respect to the MG, allowing the selected ions to travel the distance (see **figure 11**) from the MG to the interaction region. **Figure 12(C)** shows laser depletion of the anion signal and the appearance of the signal of neutral photo-detachment products that are created in the interaction region but are not decelerated as they exit the spectrometer and thus arrive $1.75\mu s$ before the parent anions.

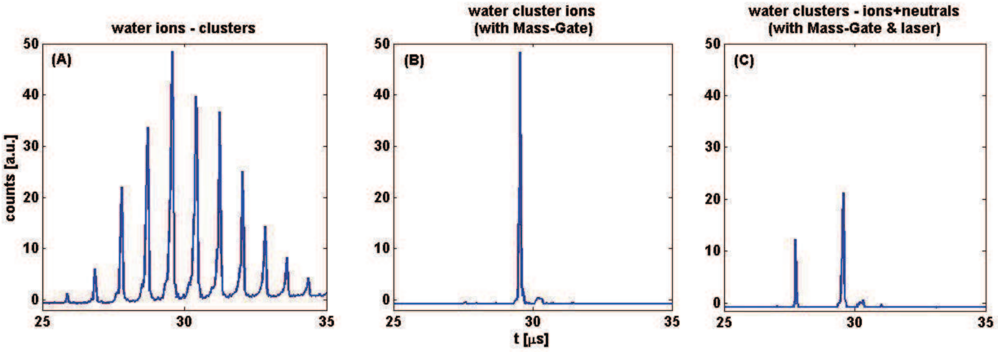

Figure 12: spectrometer operation. TOF spectrum of water clusters (used for calibration of system) without (left) and with (middle) Mass Gate. On the right is the spectrum of interaction products, with both MG and laser.

Ion trajectory simulations allow assignment of charge/mass of laser ion interaction products based on their respective TOF shifts due to the photo-fragment spectrometer. **Figure 13** shows a simulated TOF spectrum for all possible SF_6^- products from F^+ to SF_6^+, and higher degrees of ionization, as well as neutral products that are not affected by the spectrometer fields and are therefore not mass resolved and arrive with the neutral SF_6.

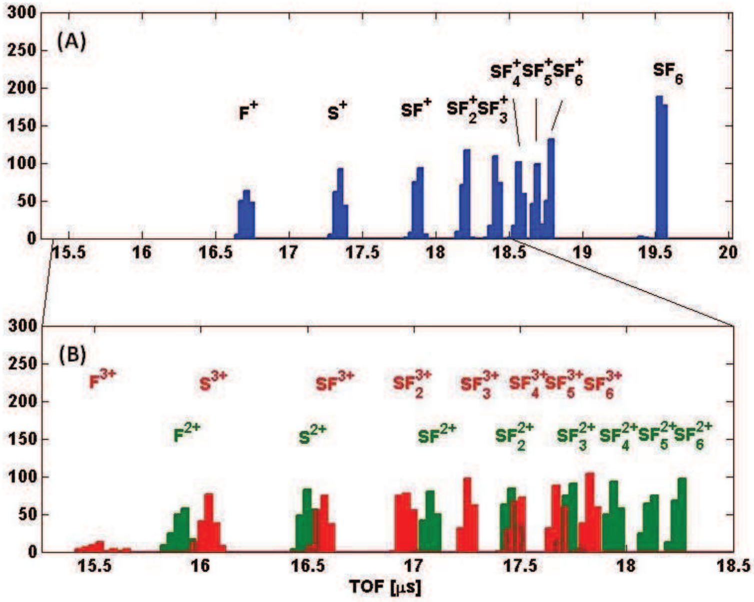

Figure 13: simulated TOF spectrum of SF_6^- photo-detachment products. The neutral SF_6 and singly ionized fragments (A) are expected to dominate the spectrum, while higher charged fragments (B) may be observed among them.

The width of the fragmented product peaks can be further broadened by the kinetic energy release (KER) in the dissociation. The energy released during the dissociation is converted to translational kinetic energy of the fragments relative to the center of mass. This results in a distribution of velocities projected on the TOF axis and hence a corresponding distribution of TOF to the detector. **Figure 14** shows simulated results of the TOF widening for two of the spectrum peaks for different values of KER with an isotropic dissociation, to be compared to experimental results.

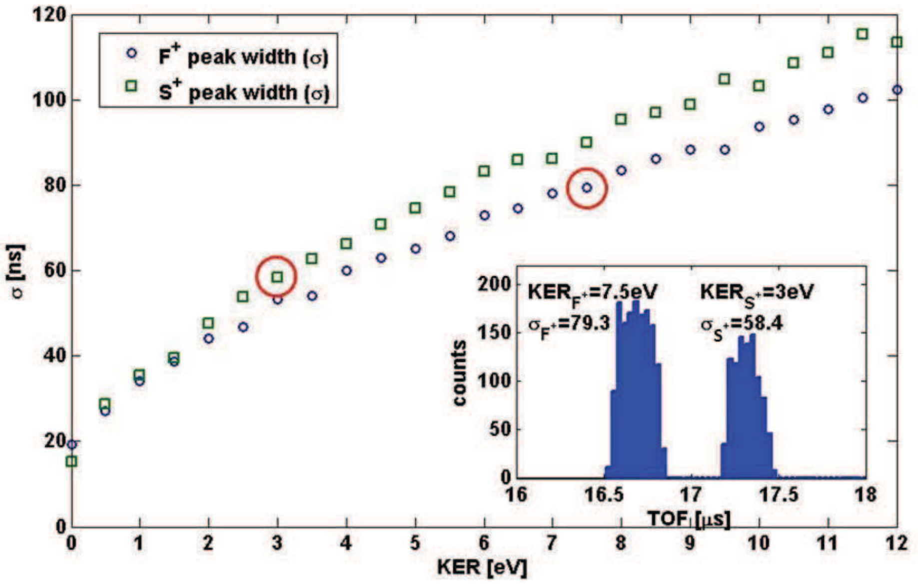

Figure 14: simulation results of peak widths (σ) for F^+ and S^+ scanning KER values. Two KER of F^+ and S^+ which will be described in the results are marked by red circles, and the corresponding spectrum is presented with appropriate peak widths (insert).

Anisotropic dissociation with respect to a laser polarization axis can lead to a different TOF peak broadening. Influence of the laser polarization stems from the tendency of ionic fragments to dissociate in alignment with the laser polarization, which is attributed to two possible mechanisms, dynamic and geometric alignment[84,85,86]. In dynamic alignment the torque exerted by the electric field on the dipole moment induced on the molecule may result in pre-alignment of the molecules to the polarization axis, enhancing the dissociation in that direction[87]. Geometric alignment refers to the efficiency of the interaction itself[84], which derives from the projection of the electric field on the un-aligned molecules dipole moment, and for linear processes amounts to an anisotropic $cos^2\theta$ distribution (θ being the angle between the dipole and the laser polarization). The anisotropy can be expected to be even larger for a non-linear process, involving n photons, where a simplistic power-law dependence on the laser power will be described by a narrow $cos^{2n}\theta$ distribution, again aligning the dissociation strongly to the laser. The difference between laser polarization parallel to the TOF axis and perpendicular polarization was simulated, comparing isotropic and anisotropic distributions, the results shown in **figure 15**. Dissociation perpendicular to the TOF axis has little effect on the TOF distribution, while on the other hand, molecular alignment parallel to the TOF axis blasts some of the fragments towards the detector, while the others dissociate away from the detector. A signature of such alignment affect is a double-peak signal corresponding to the two bunches of fragments as shown in **figure 15**.

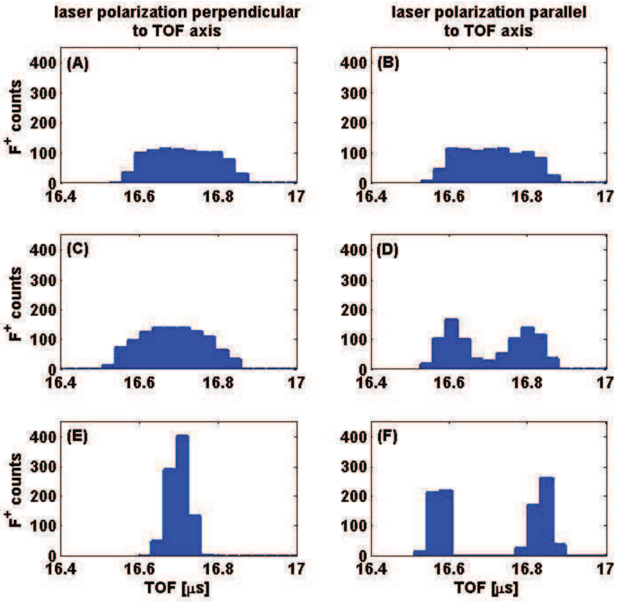

Figure 15: simulation of linear polarization perpendicular (left) and parallel (right) to the TOF axis, for the F^+ fragment, assuming 7.5 KER. For isotropic dissociation (A-B) the polarization has no affect, while for anisotropic the parallel case results in a splitting of the peak, partial for a mild anisotropic $cos^2\theta$ distribution linear case (C-D), and sharper for the 24 photon dependent ionization leading to F^+ (E-F).

4.1.4. Photo-fragment detector

As mentioned in the beginning of this chapter, our detection can record temporal and spatial hit data simultaneously. In this work, the spatial information was not utilized to its extent, but rather for optimization of the measurement. The temporal data, the TOF, is detected by a micro-channel plate (MCP), 80mm in diameter, that produces fast electronic pulses at the time of a hit. In this way we expect to be able to distinguish between the different interaction products. The MCP signal is digitized by a constant fraction discriminator and its time recorded by a Time to Digital Converter (TDC) that is read by the computer after each laser shot. The data acquisition devices and the method of analyzing the data are described in detail in Appendix D.

4.2. The laser system

In our Spectra-Physics laser system ultra-short laser pulses are generated, pulse shaped, amplified, and then introduced into the vacuum system to interact with the molecules.

4.2.1. Pulse generation

Ultrafast pulses are generated by a "Mai Tai" Ti-Saphire oscillator[78], producing laser pulses at an 80MHz repetition rate, with an average power of about 0.6W and a bandwidth of up to 85nm FWHM centered on 800nm wavelength.

Following the laser beam path depicted in **figure 5** we can next utilize a "MIIPS box 640"[88] pulse-shaper prior to amplification of the pulse. In addition to pulse compression, the pulse shaper allows to add a tailor made spectral phase that will shape the temporal envelope of the ultrafast pulses. The pulse shaper consists of a spatial light modulator (SLM), onto which the spectral components of the pulse are dispersed using a grating and focusing mirror in a 4f configuration[89]. The SLM is a double array of 128 liquid crystal cells that allows us to separately control both the phase and amplitude functions of each spectral component.

The pulse shaper is computer controlled, programmed to distort the phase, introducing chirp and TOD, by defining the coefficients (φ_2 and φ_3) of the appropriate terms. The effect of these distortions on the pulse intensity and length (normalized to a TL 40fs pulse) are summarized in **figure 16**.

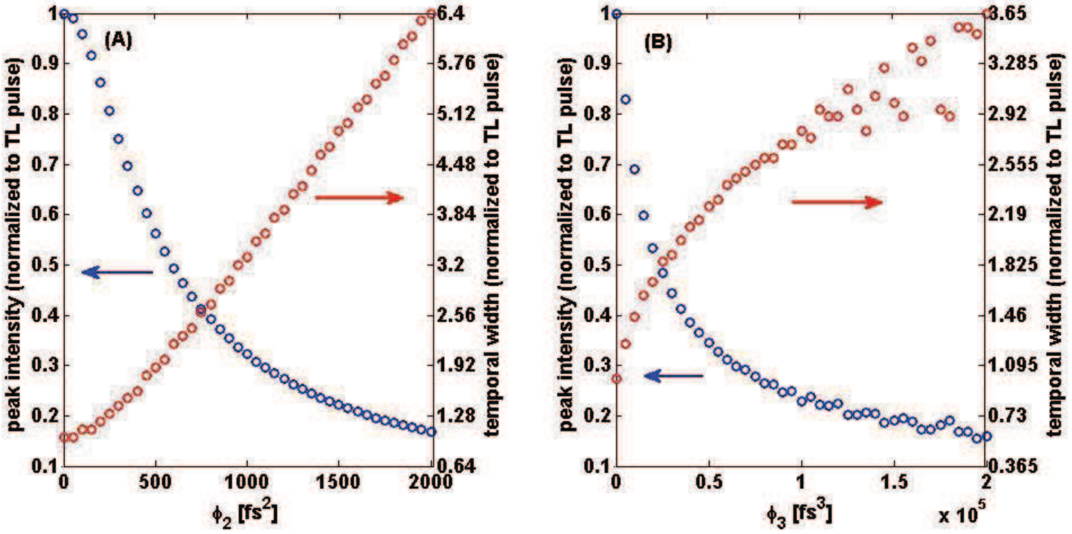

Figure 16: calculations of peak intensity (blue) and temporal width (red), both normalized to transform limited pulse, as a function of chirp (A) and TOD (B).

Next, the ultrafast pulses are amplified at a kHz repetition rate in the "Spitfire Pro XP" regenerative amplifier[79], which is pumped by a Q-switched Nd:YLF laser, "Empower"[90], pumping 17W pulses. Prior amplification, the ultrafast pulses are stretched in time by dispersing them along the beam path using a grating stretcher. This is preformed to prevent possible damage to the optical devices with the intensity of a fully compressed pulse. After amplification the pulses are compressed by applying inverse dispersion with a grating compressor. At the output of the amplifier 3.2mJ pulses with 40nm FWHM bandwidth and a waist of 4.35mm are compressed to about 35fs.

4.2.2. Additional beam manipulation

In addition to controlling the shape of the pulse, we perform several manipulations on the polarization and power of the pulses before they interact with the ions. The angle of laser polarization is continuously tuned by a computer controlled rotation of a half-wave plate that rotates the polarization of the laser. Placing a thin-film polarizer in the beam path as illustrated in **figure 5**, which transmits only P polarization, we are able to tune the power of the pulse by rotating the polarization axis. Power attenuation performed in this manner assures that peak intensity is changed without affecting the original pulse shape. Alternatively, a quarter-wave plate can be positioned in the beam path, allowing us to manipulate the polarization ellipticity, from linear to circular polarization.

As seen in **figure 5**, before entering the vacuum system our beam is focused into the vacuum chamber to achieve intensities typical for non-linear processes. We evaluate the pulse energy in the interaction zone to be about 2.2mJ, and a slight elongation of the pulse to about 40fs. Using a 250mm focal length lens, focusing an 800nm pulse down to 14.6μm is theoretically reachable, corresponding to intensities of a few tens of PW/cm^2. We mount the lens on a translation stage, with an effective range of 20mm, and controlled by our computer program. The high dependence of our process on the intensity makes tunability of the intensity an important tool, though optical phenomena can affect a manipulated laser pulse, in turn affecting the exact intensity achieved. The characterization of both temporal and spatial focusing, which affects the intensity, is described in chapter 5.

4.3. Synchronization

All the devices described in this section are synchronized, in order to control and measure the desired molecules. In this way, we time the e-gun and accelerator to influence only a limited portion of the particle cloud, to be then again restricted to a single mass by the pulsed mass gate. These devices are timed by using switches, which are in turn synchronized by the computer program that controls the devices, determining delays and operation time lengths with a Data Acquisition System (DAQ). The initial trigger to all devices is the laser itself which triggers the Pulsed Valve (PV) who starts the chain of events. Since the laser is both the trigger and a player in the interaction during the ion flight, the PV is delayed to bring the ions to the interaction zone in time for the next laser pulse (who triggered the next ion bunch etc.) to arrive at the system. The falling edge of this switch (determined by the length) is further on used to time the TDC for cleaner data acquisition.

Figure 17 shows a typical timing scheme implemented by 4 programmable timer/counters that control the relative timing of different stages of the experiment and are all synchronized to the laser timing signal.

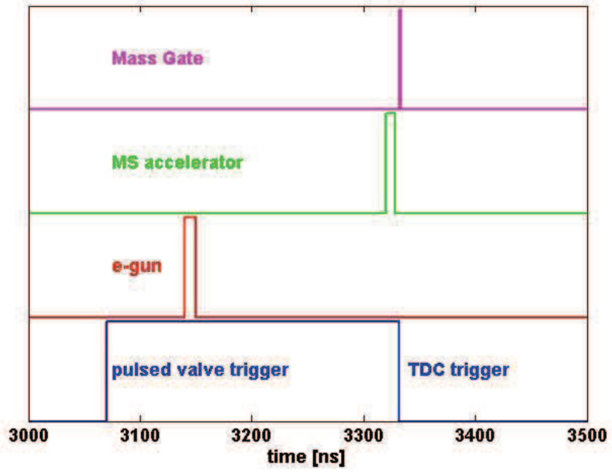

Figure 17: time scheme of the different power supplied devices, synchronized to produce and measure the desired product. The time profiles reflect the activation of the switches themselves and not the voltage amplitudes of the devices they control. The switch triggered by the laser uses the rising edge to trigger the pulsed valve and the falling edge for the TDC recordings.

The appropriate timing of the devices has a crucial role in obtaining a good signal, by optimizing the overlap in the interaction zone and the resolution at the detector. The synchronization of the laser to the ion beam propagating in the vacuum system enables the interaction between the two at optimal timing. A photo-diode measuring the generated laser pulse serves as a trigger for the vacuum system's chain of events. The short (especially when temporally focused by the W.M. accelerator), fast-moving ion beam requires synchronization of the laser and vacuum systems to the order of nanoseconds. **Figure 18** emphasizes this argument, and shows a scan in which the laser delay is tuned (as a result of changing the PV triggering delay, effectively changing the synchronization with the next laser pulse). From the scan profile a FWHM time window of 50ns is measured to produce an interaction signal. From a velocity of 50km$\cdot$sec^{-1}, the length of the ion beam is calculated to be a few mm long, the asymmetry of the scan profile resulting from a non-uniform distribution of the ion bunch.

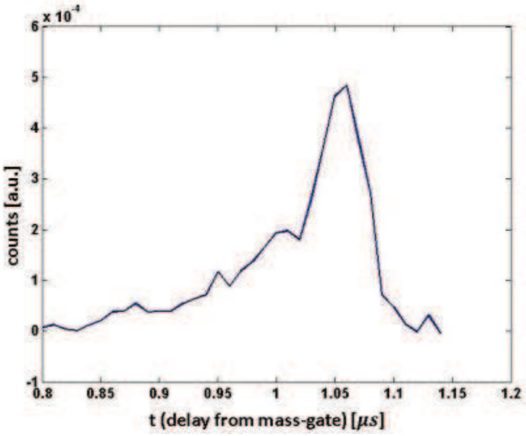

Figure 18: laser delay scan tuning interaction to different spots along the ion beam, enabling to quantify the ion bunch length. Here, a short ion beam, focused in the interaction zone, is measured to be a few mm long.

5. Beam characterization

Our experiments involve non-linear processes that are strongly dependent on the peak intensity of the laser electric field driving the process. While laser pulse energy can be determined by measuring the average laser power divided by the laser repetition rate, calculation of the peak intensity requires detailed characterization of the spatial and temporal profile of the laser pulse at the laser-ion interaction region.

5.1. Theoretical background

The spatial mode of our laser beam can be ideally described as a Gaussian beam, which as shown in **equation 15** can be described by its waist, w, and peak intensity I_0, related to the total power P_0 of the laser beam through $I_0 = \frac{2P_0}{\pi \cdot w(z)^2}$.

(15) $$I(x,y;z) = I_0 exp(-\frac{2\cdot(x^2+y^2)}{w(z)^2})$$

It can be shown that the focusing of a Gaussian laser beam is limited to

(16) $$w_0 = \frac{\mathrm{\lambda \cdot F}}{\mathrm{\pi \cdot D}}$$

where D is the waist of the collimated laser, F is the lens focal length and λ is the wavelength. The change in the beam waist as a function of distance from the focal point, $w(z)$, is described in **equation 17**, where the Rayleigh range, $\mathrm{z_R}$, is given by $\mathrm{z_R} = \frac{\mathrm{\pi \cdot w_0}^2}{\lambda}$ and expresses the distance from the focal point at which the laser area is doubled.

(17) $$w(\mathrm{z}) = w_0\sqrt{1+(\frac{\mathrm{z}}{\mathrm{z_R}})^2}$$

To describe the focusing of a realistic non-Gaussian laser beam, a M^2 factor is introduced to scale the actual beam waist at the focal point[91]:

(18) $$\widetilde{w}(\mathrm{z}) = M^2 \cdot w_0\sqrt{1+\left(\frac{\mathrm{z}}{\mathrm{\tilde{z}_R}}\right)^2}$$

The Rayleigh range is similarly rescaled to $\mathrm{\tilde{z}_R} \equiv M^2 \mathrm{z}_R$. For $M^2 = 1$ **equation 18** reduces into **equation 17**, while for a $M^2 > 1$ one can see that the minimal beam waist will increase by a factor of M^2, thus not reaching the theoretical focusing limit of a Gaussian beam, as illustrated in **figure 19**.

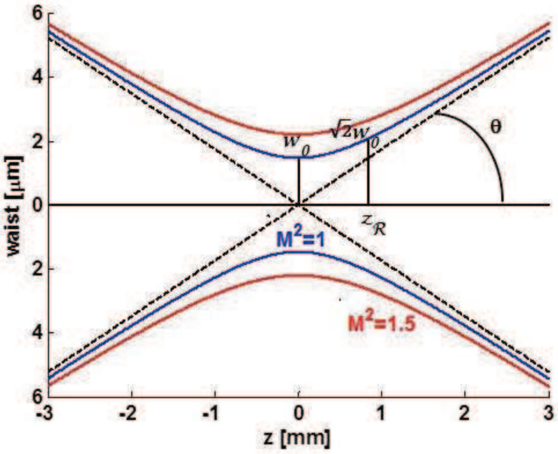

Figure 19: illustration of beam size while focusing to a minimal waist, w_0, and then defocusing. The waist is calculated for a TL pulse ($M^2 = 1$), and for a distorted pulse with $M^2 = 1.5$.

The M^2 can also be defined[92] by the half-divergence angle $\theta = \frac{D}{F}$ through the relation $M^2 = \frac{\pi \widetilde{w}_0 \theta}{\lambda}$.

5.2. Spatial focusing measurements

We performed direct measurements of the size and shape of the laser beam in a dedicated beam characterization setup that we constructed outside the vacuum chamber. Measurements were performed by attenuating the laser beam by more than 10 orders of magnitude and directing it onto a CCD camera chip, located at the same optical path length as the laser-ion interaction region. **Figure 20** shows the result of the $M^2 = 1.5$ fit to average beam waist, as well as more detailed analysis indicating the origin of the deviation from Gaussian beam is due to a small astigmatism in the laser beam (insert CCD images). Astigmatism is the occurrence of two perpendicular axes of a beam that differ in foci. Since the two do not focus to their minimum width at the same point of a focal distance scan, the measured width would be elongated between the two points at a geometrical average width, larger than the expected one. Reconstructing the intensity profile from the CCD images enables extraction of the beam widths for both axes of the beam as shown in the figure, from which about 1.5 mm deviation of the focal point in the X and Y directions can be concluded.

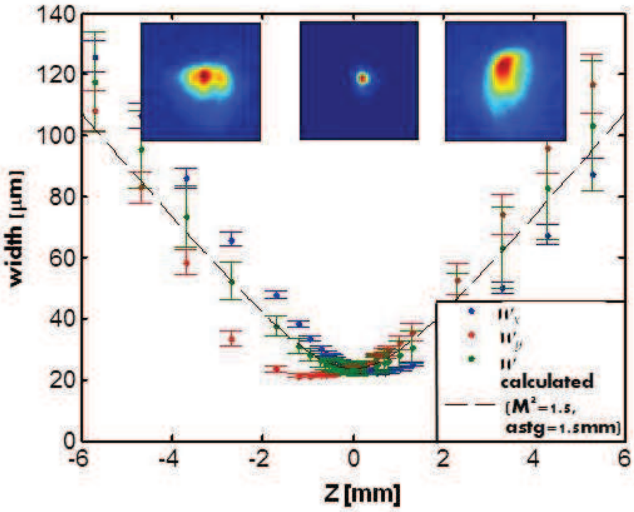

Figure 20: the results of a focus scan, separately for two axes of the pulse front, as measured by a CCD camera. The effective width is calculated by $w = \sqrt{{w_x}^2 + {w_y}^2}$ and compared to the theoretical width expected with an $M^2 = 1.5$, and the apparent astigmatism of 1.5mm difference between the foci of each axis (dashed line).

5.3. *In situ* laser focusing measurements

In addition to the laser profile measurements performed outside of the vacuum system, we performed *in situ* characterization of the laser focusing in the actual interaction region with the molecular ions, using measurements of linear photo-detachment processes. The molecular systems we used for this experiment are water cluster anions corresponding to the following photo-detachment process:

$$(H_2O)_n{}^- + h\nu \rightarrow (H_2O)_n + e^-$$

The binding energy of water is close to 1.2eV[93] that is lower than the average 1.5eV photon energy corresponding to our 800nm laser, thus being a good candidate for the linear process. Using this molecule, while changing the lens position, and the degree of focusing in the interaction zone, we wish to learn the actual lens position at which the laser is focused at the interaction region and the realistic focusing of the laser beam inside the vacuum system.

In a linear photo-detachment process one can expect the neutral product yield to follow **equation 19**, where the molecular detachment yield depends on the detachment cross section (σ) and the photon flux (Φ) which is the pulse energy divided by the photon energy and the beam area. The yield also depends linearly on the ion density and overlap volume between the ion beam and the laser

($\mathrm{N_{ion}}$, $\mathrm{F_{overlap}}$ respectively), which multiplication gives the total ion population that interacts with the laser pulse.

(19) $$yield = \mathrm{N_{ion}} \cdot \mathrm{F_{overlap}} \cdot (1 - \mathrm{e}^{-\sigma \cdot \Phi})$$

Using this equation and assuming that only linear processes contribute to the measured signal, we can calculate the expected yield as a function of laser focusing. Simplifying **equation 19**, we see that at the high photon flux limit the yield is sensitive to the overlap volume alone:

(20) $$yield \cong \begin{cases} \mathrm{N_{ion}} \cdot \mathrm{F_{overlap}}\ ; & \sigma \cdot \Phi \gg 1 \\ \mathrm{N_{ion}} \cdot \mathrm{F_{overlap}} \cdot \sigma \cdot \Phi; & \sigma \cdot \Phi \ll 1 \end{cases}$$

The second limit reflects the case of low power, where we expect a linear dependence on the flux, or the power. **Figure 21** shows the detachment yield measured with a focused beam for different attenuations of the power, and the two limits are observed. We verify being in the saturated case of the high flux limit, and using **equation 19** we estimate a reasonable cross section of 1Mb, typical for cross sections of these laser energies.

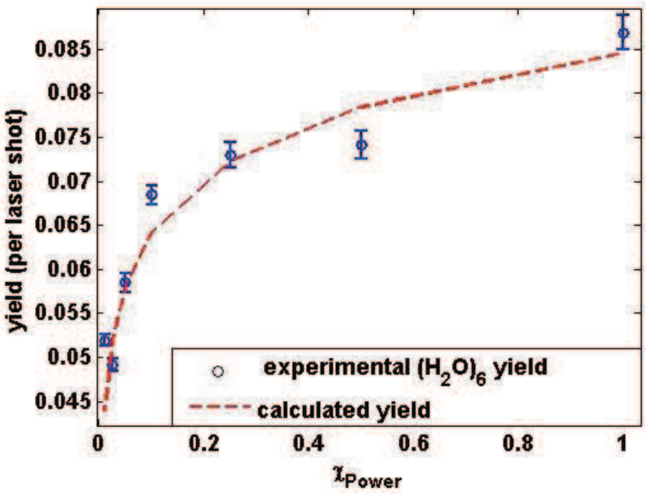

Figure 21: a power attenuation scan (here done not by the polarizer device but rather with ND filters). The scan indicates that, when not attenuated, we are in the saturation regime for this process.

One can expect that for a linear process, product yield will drop to a minimum when the laser is focused at the interaction region with the ion beam target, due to the decrease in overlap volume. By measuring the detachment yield while moving the lens position, thus changing the focusing at the interaction zone, we can determine the lens position corresponding to focusing the laser beam in the midst of the ion bunch. In **figure 22** we compare calculation results to the $(H_2O)_6^-$ photo-detachment yield and we find calculation and data to be consistent with a depletion cross section of about 1Mb as deduced by the power scan.

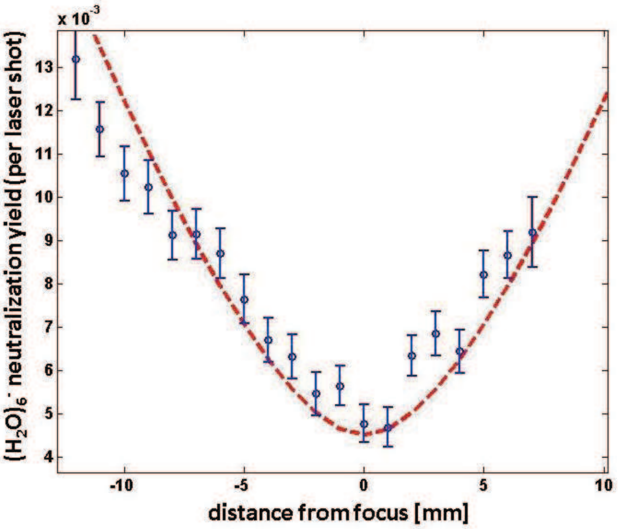

Figure 22: a comparison of experimental and calculated trends for the focusing scan, with all phenomena taken for account, including a weak (8% power) reflected beam which due to the wide spread it accumulates is enough to execute the linear process measured. The calculations make use of **equations (15,19)**, assuming a cross-section of 1Mb.

The calculations based on **equation 19** took into account additional experimental geometric factors, such as the ~5mm width of the ion beam, throughout which the laser intensity varies. Also the length of the ion bunch, focused by the Wiley-McLaren method described in the previous chapter, was measured to ensure it is long enough to maximize the overlap with the laser. Furthermore, SIMION simulations verify maximum product yield for different ion bunch diameters governed by the focusing einzel lens, ruling out the possibility of a wide beam being blocked in the path of flight. In order to fit measured data, we also include in the simulation a reflection of 8% of the laser power from the exit window, a reasonable value for the double-layered, uncoated, fused silica window, as implied by manufacture specifications[94]. This reflection is not expected to be significant for non-linear processes, but has to be considered for analysis of linear phenomena

Equation 19 is generally typical of linear photo-detachment, and is indifferent to the species measured. Several cluster sizes, as well as atomic O^- anion were tested, as shown in **figure 23**, in order to exclude experimental artifacts caused by significant molecular fragmentation that may occur due to the water cluster size.

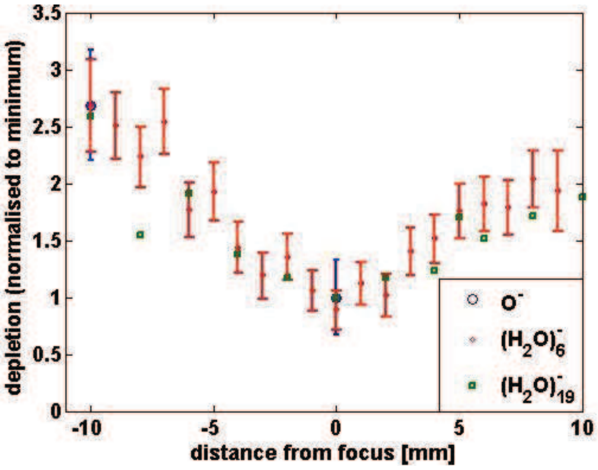

Figure 23: adjusting the motorized stage position we move the mounted lens to different distances from the interaction zone. From the measured neutralization signal we find the focusing position expected to yield minimal signal. Repeating this kind of scan for several molecules differing in size we rule out a contribution from fragmentation.

Furthermore, the assumption of a predominantly linear laser-ion interaction even at an extremely focused beam was confirmed by showing chirp dependence. **Figure 24** shows a scan of the detachment yield of $(H_2O)_6^-$ as a function of compressor stage position, that stretches the pulse in time and suppresses non-linear phenomena while having no effect on linear processes. The linear photo-detachment of the water cluster anion is compared to the non-linear ionization of the residual gas molecules.

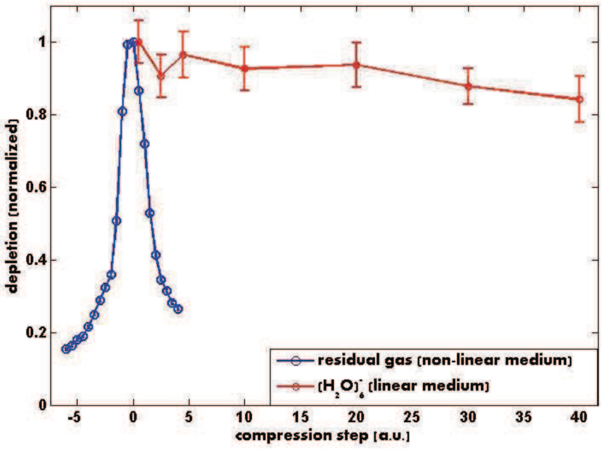

Figure 24: results of a chirp scan (here with crude steps using the Spit-Fire compressor). The constant trend corresponding to a linear process is emphasized in comparison to the strong dependence of the non-linear process relevant to the RG ionization.

5.4. Temporal focusing measurements

Measurements of the temporal width of ultra-short pulses are not possible using standard electronic devices, since the time resolution of these equipment is limited to the ns scale of electronics. The conventional method is therefore an auto-correlation (AC) measurement. In this type of measurement, illustrated in **figure 25(B)**, a beam splitter is used to create two replica of the laser pulse and direct them through the two arms of a Michelson Interferometer. The two beams are combined in a second harmonic generation (SHG) crystal and their relative time delay is computer controlled by a translation stage that changes the optical path of one arm of the interferometer. The SHG signal is measured using a two-photon diode as a function of time delay between the two replicas of the pulse. As the SHG process is proportional to the square of the instantaneous intensity of the light field, the yield depends on the temporal overlap between the two pulses, and the resulting interferogram allows determining the duration of the pulse. **Figure 25(A)** shows two types of AC measurements, the blue line shows an interferometric auto-correlation measurement in which the two beam paths are perfectly co-linear, allowing us to observe the interferences of the carrier frequency of the laser pulse. The red dots correspond to a non-interferometric measurement, which is obtained by introducing a finite small angle between the two beam paths, and is sensitive only to the temporal envelope of the pulse and not to its carrier frequency. Analysis of both methods by assuming a Gaussian like pulse shape allows to determine a pulse duration of 42fs FWHM.

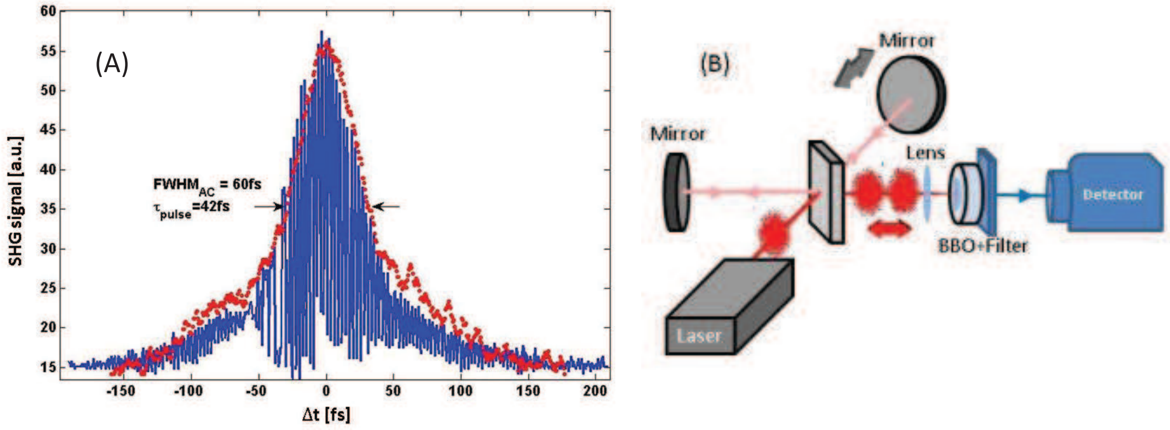

Figure 25: an interferometric auto correlation measurement of the pulse with itself in a collinear configuration (B). This scheme restores most of the field phase properties except at the fringes (A-blue). The 60fs FWHM extracted from the results of an AC (not co-linear) measurement (A-red) can be de-convoluted to give the 42fs width of the original pulse.

We also take advantage of our pulse shaper in order to characterize not only the time duration of the pulse but also its phase, by implementing the Multiphoton Intrapulse Interference Phase Scan (MIIPS)[95]. Briefly, in this technique SHG spectrum of a single pulse is recorded as a function of a sinusoidal spectral phase of the form $f(\omega,\delta) = \alpha \sin(\gamma\omega - \delta)$ written by the pulse shaper in addition to the spectral phase of the unshaped pulse $\Phi(\omega)$. **Figure 26** shows the measured SHG spectra as a function of the δ offset of the spectral phase. For each wavelength, the maximal SHG yield is obtained for a vanishing second derivative of the overall spectral phase, a condition which is satisfied when $\Phi''(\omega) = -f''(\omega)$. Therefore, for a given $\delta_{max}(\omega)$, one can determine the spectral phase by integrating **equation 21**:

(21) $$\Phi''(\omega) = \alpha\gamma^2 sin\,(\gamma\omega - \delta_{max}(\omega))$$

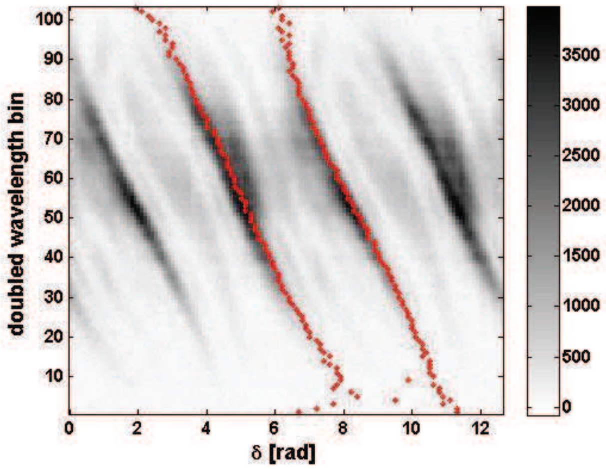

Figure 26: the 2D result of a MIIPS scan of the SHG signal, as a function of the spectral phase shift δ. The red dots follow $\delta_{max}(\omega)$, from which we reconstruct the phase, and correct to get a non-distorted pulse.

The Fourier transform of the combined measurement of the spectral intensity and spectral phase allows determining the actual temporal pulse shape. **Figure 27** shows the MIIPS results of spectral intensity and phase, and the corresponding temporal pulse shape with a pulse duration of about 43fs.

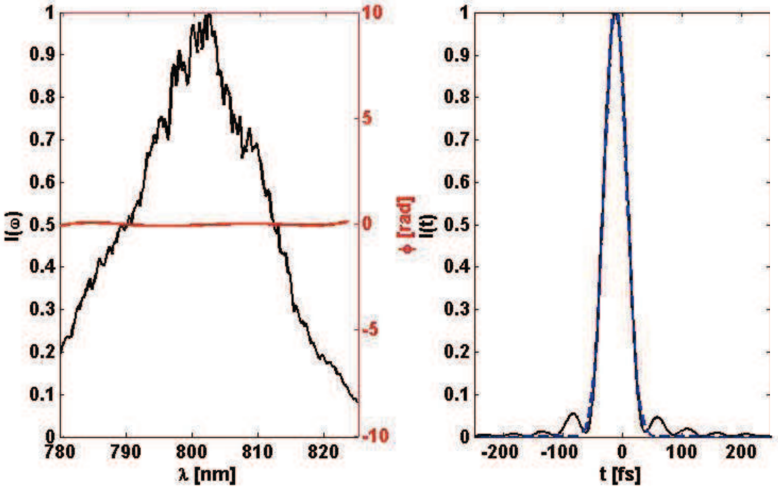

Figure 27: MIIPS results of spectral intensity and phase (A), and temporal pulse shape (B). The shape is Gaussian-like as can be seen from the dashed fit (blue), the side lobes a consequence of our limited spectral range.

5.5. Intensity calculation

Based on the spatial and temporal characterizations of the laser pulse, it is possible to evaluate the peak intensities at the interaction region corresponding to the displacement of the focusing lens as shown in **Figure 28**. The effective beam waist at each lens position, also presented in the figure, takes into account the distortion of our beam expressed by the M^2 factor, and astigmatism resulting with an elliptically shaped beam. The pulse duration, Δ_t, as determined by our temporal focusing measurements may be modified as described by **figure 16** in section 4.2.1. The beam waist and time duration are used to calculate the instantaneous peak intensity for given focus distance z, and pulse energy U, through $I_0(z) = \frac{U}{\Delta_t \cdot \pi \cdot w_x(z) \cdot w_y(z)}$.

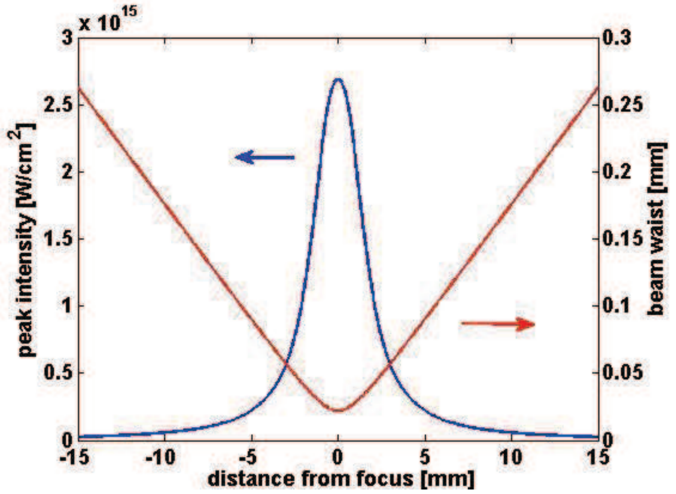

Figure 28: the peak intensity and beam waist as a function of focusing, for a 2.2mJ pulse, with temporal length of 40fs.

6. Results and discussion

In the following I describe the investigation of anionic SF_6^- molecule interaction with intense laser pulses. **Figure 29** shows a typical TOF spectrum corresponding to the interaction of SF_6^- with a 10^{14}W/cm^2 intense laser pulse (and for higher intensity in insert). The TOF spectrum allows identifying the different products of the interaction with intense laser pulses, based on their charge to mass ratio.

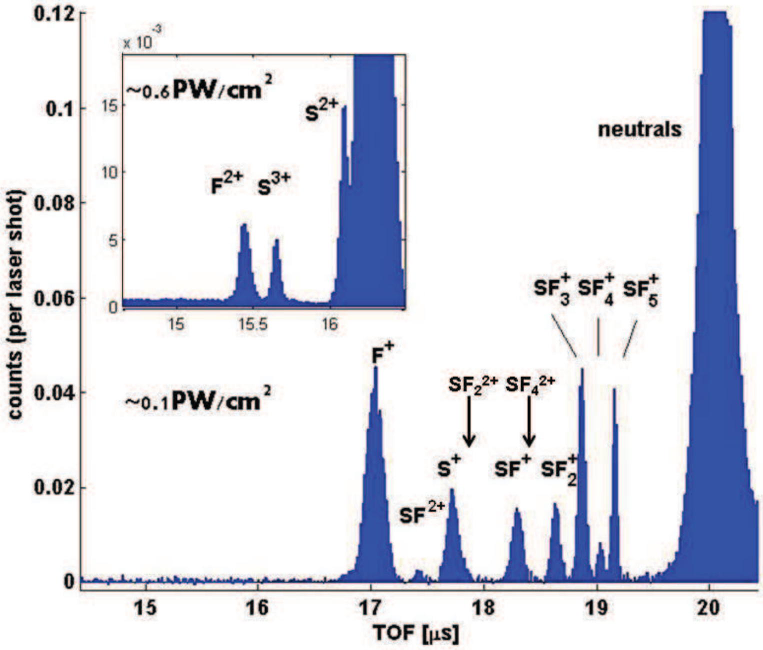

Figure 29: a TOF spectrum typical of a moderate intensity of 10^{14}W/cm^2 yielding multi-photo detachment products. The neutralization product is clearly visible as well as the singly ionized fragments. The higher ionization fragments appear at higher intensities (in insert - measured using higher spectrometer voltages, hence the different times).

The dominant peak in the TOF signal corresponds to neutral products that are predominantly due to SF_6 produced by single photo-detachment. Other channels, leading to dissociation also produce neutral fragments that arrive at a similar TOF. However, we expect that at the intensity shown in **figure 29** the neutral product peak is dominated by detachment of a single electron. The smaller TOF peaks correspond to cationic fragments that are resolved according to their charge over mass ratio, allowing a clear identification of double- as well as multiple-detachment processes. All the possible stable cations are observed from atomic F^+ and S^+, until molecular SF_n^+ ions, n ranging from 1 to 5, while the unstable SF_6^+ is not detected.

Interestingly, the cation spectra are found similar to those resulting from intense field ionization of neutral SF_6 molecules[96]. A prominent feature is the absence of the evidently unstable SF_6^+ cation[97], that dissociates and contributes to the fragmentation spectrum. Another feature is the alternating signal strength, as higher yields of odd-number fluorinated fragments, especially the SF_3^+ and SF_5^+ fragments[56] are observed. The selectivity for some fragments over others is also qualitatively understood in terms of the stability of the different species, due to the sulfur hybridization considerations derived from the simplistic valence-bond theory[38]. This explanation further predicts the opposite behavior of the doubly ionized fragments, as was noted in intense field ionization of neutral SF_6 measurements[38], where SF_2^{2+} and SF_4^{2+} showed higher yields. Under our conditions SF_2^{2+} and SF_4^{2+} are expected to overlap with S^+ and SF^+ peaks respectively, thus small doubly-ionized signal may well be obscured. We therefore are not able to observe this feature, though the peaks might be hinted by the longer TOF tails of the S^+ and SF^+ peaks.

For the higher intensities, shown in the insert of **figure 29**, multiply charged atomic species are clearly observed with charge states of up to F^{2+} and S^{3+}. The measured TOF spectra of fragments can also be analyzed in terms of kinetic energy release (KER) that leads to the observed broadening of TOF peaks, especially for the lighter F^+ fragments as can be seen in **figure 29**. From comparing the peak widths (80±2ns for F^+ and 58±3ns for S^+) to our simulations presented in chapter 4, we can conclude that the F^+ and S^+ are emitted with about 7.5±1.5eV and 3±1eV KER respectively. Such high KER can originate from Coulomb explosion of highly charged parent ions, releasing high energy in the dissociation due to the Coulomb repulsion between charged fragments[75]. The large errors are suggested following our uncertainty in the isotropy of the dissociation (see below), and the small TOF discrepancies from simulation. In **figure 30** we show a comparison with TOF spectra collected with the laser polarization rotated parallel and perpendicular to the direction of the TOF axis, showing similar broadening and peak intensity indicating that fragment emission in all directions is detected on our detector. This feature validates our detection capabilities in terms of the detector acceptance, particularly in perpendicular polarization which may blast the fragments away from the TOF axis leading to low efficiency of detection when using small detectors with low acceptance.

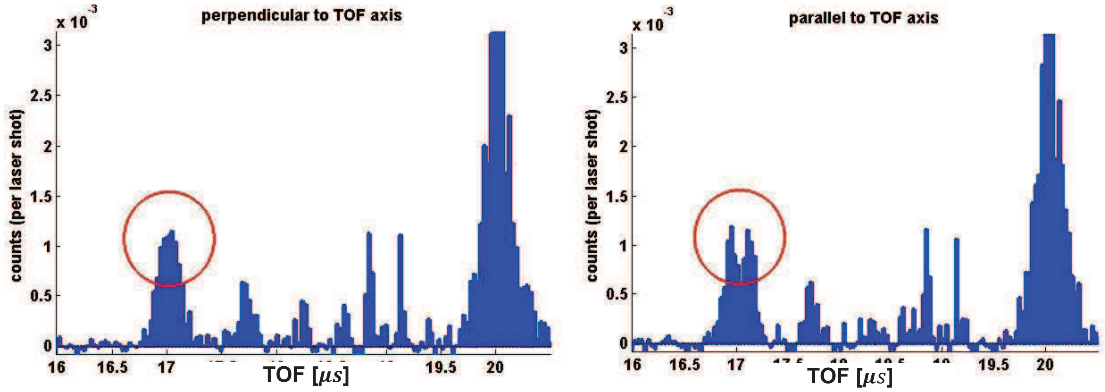

Figure 30: a TOF spectra with laser polarization perpendicular and parallel to the TOF axis. The dissociation is enhanced in the axis of polarization leading in the parallel case to two groups of F^+ fragments recognized by the splitting of the signal. The background noise originated by residual gas cations, is enhanced as well in this case, as the KER burst assists in passing the a-symmetric barrier.

Comparing the parallel and perpendicular spectra to the simulation results presented in **figure 15** (chapter 4.1.3), we conclude that the observed anisotropy in the F^+ emission is even less prominent than the simulated spectra for a one-photon dissociation along the dipole moment axis. Subtle anisotropy is perhaps not surprising, considering the octahedral structure of SF_6. Recent calculations of the anionic SF_6^- that indicate deviations from octahedral symmetry[55], may explain the subtle splitting through either dynamic alignment of the molecule by the laser pulse, or through geometric enhancement of the dissociation parallel to the laser polarization starting from an anisotropic initial distribution.

The KER we deduced is larger than the 5eV KER attributed to F^+ by previous groups[98] performing multiple ionization of neutral SF_6 by intense laser fields. Both results imply the occurrence of a coulomb explosion, and the different KER may be attributed to the different molecule systems, neutral and anionic. Extraction of geometric structure from photo-detachment KER data is very hard for complex molecules like SF_6, that do not fit simplistic models like those referred to by **equation**

11, and that correspond to multi-detachment processes and multiple channels of dissociation.

In order to obtain a better understanding of the KER and anisotropy of the emission, future coincidence and position-sensitive measurements that are beyond the scope of this thesis are on their way.

In the following sections, the yield of the different possible channels of single, double and multiple detachments are presented as a function of experimental parameters, such as focusing, total power and phase distortions. With that we wish to resolve to some extent the mechanism of these processes, and to outline the differences between anionic systems and the widely investigated neutral molecules. Both the different charged states produced by the photo-detachment process, and the cationic fragments resulting from dissociation and coulomb explosion will be considered.

6.1. Focusing dependence

The non-linear interactions of interest are highly sensitive to the laser field intensity that is determined by the spatial focusing of the laser beam at the laser-ion interaction region. Therefore, the first step in determining good working parameters for intense laser-ion interaction measurements is identification of favorable focusing conditions, that offer a good balance between the peak intensity required for the non-linear processes and the interaction volume that is reduced as the laser spot is focused.

Figure 31 shows the yield of different product charge states as a function of lens position that varies the size of the laser spot at the laser-ion interaction region. In contrast to the focusing scan profile of linear processes that was shown in the previous section, the non-linear nature of the interaction manifests itself in the increase of product yields as the laser spot is focused and peak intensities increase as the focal point is approached from infinity. This trend is reversed at the point at which the non-linear dependence of the process on peak intensity is balanced by the volume effect. **Figure 31** clearly shows that the yields of neutral, singly and multiply ionized products reach this balance at increasing peak intensities of about 0.04, 0.6 and 2 PW/cm^2 respectively. The clear trend can be understood, considering the higher number of photons that are needed to reach increasingly ionized species. The branching ratios (BR) between the different charge states, as shown in **figure 32(A)**, reflect how the dominance of the different species change with increasing peak intensity.

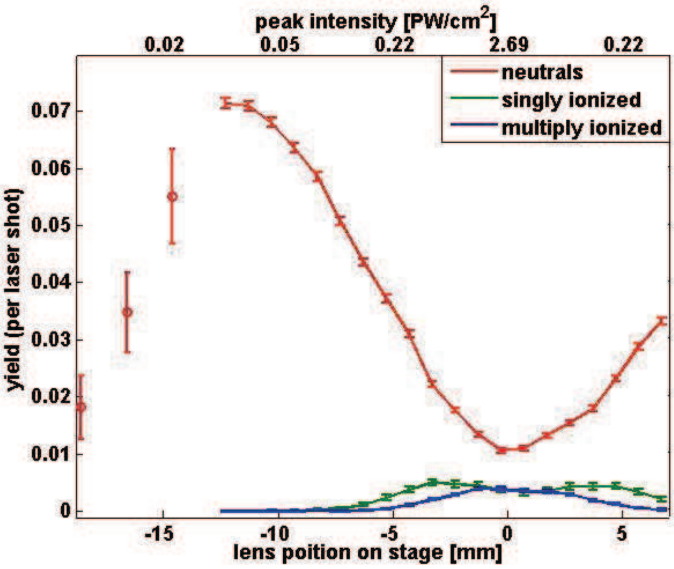

Figure 31: a focus scan profile of the different charge state products. The balance between intensity and volume considerations is clearly observed, and is shifted between the different products.

In addition to charge state characterization, our technique allows to resolve the charge over mass ratio, thus resolving the charged products also by their mass. **Figure 32(B)** shows the BR of the different singly charged cationic fragments. As could be expected, the BR of products with higher appearance energies, as listed in **table 1**, increases with increasing peak intensities, completing a transition from cation spectrum dominated by molecular products at 5x10^{13} W/cm^2 to a spectrum dominated by atomic cations at 1.5x10^{14} W/cm^2. Interestingly, it seems that for higher intensities, the BR remains constant, although the relative yield of cationic products (shown in **figure 32(A)**) continues to increase.

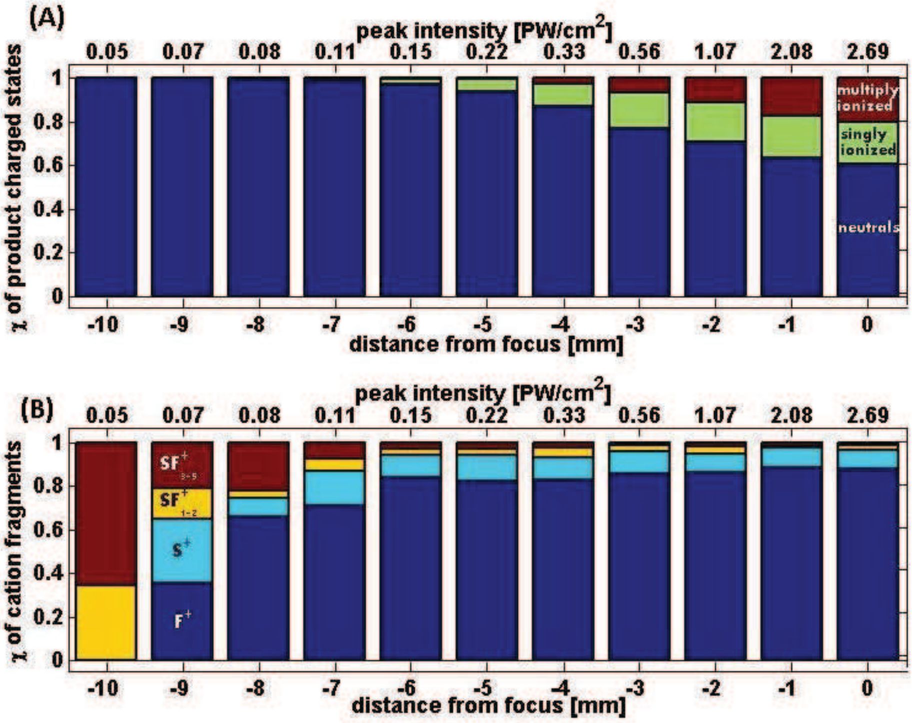

Figure 32: the branching ratio of the different charge state products (A), and the different singly ionized fragments (B). Investigating multiple ionization products requires working at high focusing conditions, while moderate focusing enables the examination of the fragmentation channels.

The apparent crossing between dominance of the larger molecular fragments to fully fragmented atomic cations, as the intensity increases, led us to continue and explore in more detail the double and multiple detachment mechanism at a focal distance of 7mm (1.15x10^{14} W/cm^2).

6.2. Power dependence

In simple cases, non-linear laser induced processes will have a power law dependence on the laser intensity[10]. Continuous tuning of the total laser power, thus changing laser intensity without affecting other parameters such as pulse length or ion-laser interaction volume, was achieved using computer controlled rotation of a broadband half-wave plate in front of a broadband thin-film polarizer. Opposed to other pulse attenuation methods, this method allows us to control total power without affecting the focusing, pointing and pulse shape. It should be kept in mind, though, that despite retaining the total width of the pulse, the overall power is reduced, thus changing the time required for the pulse to achieve a given intensity.

Equation 23 shows that using a log-log scaling, a power law product yield dependence on the laser intensity is transformed into a linear dependence with the slope corresponding to the power of the process. In more complicated cases we can expect the onset of higher order processes with increasing intensity to appear as a positive curvature in a log-log plot (increase of local slope at higher intensities), while saturation of a process, for example due to parent ion depletion, can be expected to result in a negative curvature, eventually leading to a constant maximal yield at high enough intensities.

$$\textbf{(23)} \qquad yield(I) = AI^{\nu} \qquad \rightarrow \qquad \log(yield) = \nu \cdot \log(I) + \log(A)$$

The log-log plot in **Figure 33(A)** shows the clear signature of saturation in the yield of neutral products as a function of total power of the laser pulse. Henkin *et al*[99] proposed that due to the Gaussian shape of the laser beam, we can estimate the saturation intensity by extrapolating the linear trend of the saturated yield when plotted against $\log I$. As illustrated in fig **33(B)**, saturation intensity is reached already at few 10^{13}W/cm^2, making it difficult to reliably extract the power dependence of the neutral product yield.

The 1.5 power-law extracted from the power scan as shown in **Figure 33(A)** may indicate saturation effects even at intensities that precede saturation of the interaction volume. If the neutralization of SF_6^- requires two photons, as expected from the vertical route, and an intermediate state is involved, the initial excitation may be saturated even if not all anions continue to be neutralized. This would appear as if less than two photons take part in the process and in a power-law smaller than two. Otherwise, the 1.5 slope may be attributed to the contribution of an indirect excitation to an excited state leading to auto-ionization, which may require only one photon. Furthermore, the saturation intensity of 22.7TW/cm^2, as depicted in **figure 33(B),** is actually compatible to the intensity at which the Keldysh parameter for tunnel ionization through the vertical detachment energy of SF_6^- (see chapter 2.3 **table 2**). We can therefore conclude that tunneling is an important mechanism at high intensities.

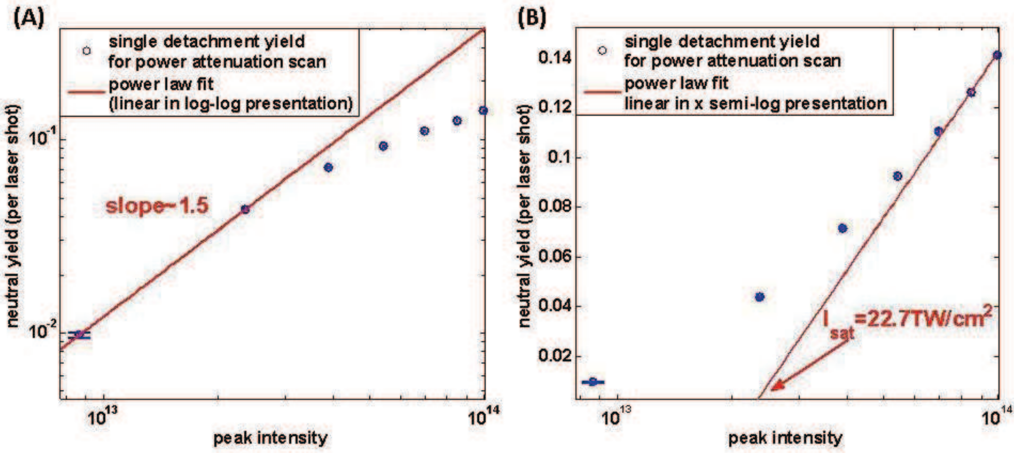

Figure 33: a log-log plot of the product yield dependence on the intensity resolves the power law attributed to the process (A). This analysis must be done within the non-saturated regime. The top limit of this regime can be evaluated from the curvature of the plot, or by the technique proposed by Henkin *et al* (B).

In contrast, the yields of cations shown in **figure 34** do not seem to suffer from saturation in the studied range of intensities. The difference can be understood as due to the higher energy required, and consequently lower probability for occurrence of a multiple ionization process. Assuming a power-law dependence on the laser power, with the exponent reflecting the non-linearity, or the number of photons involved in the reaction, the higher power laws mentioned in **figure 34** indicate higher energies involved.

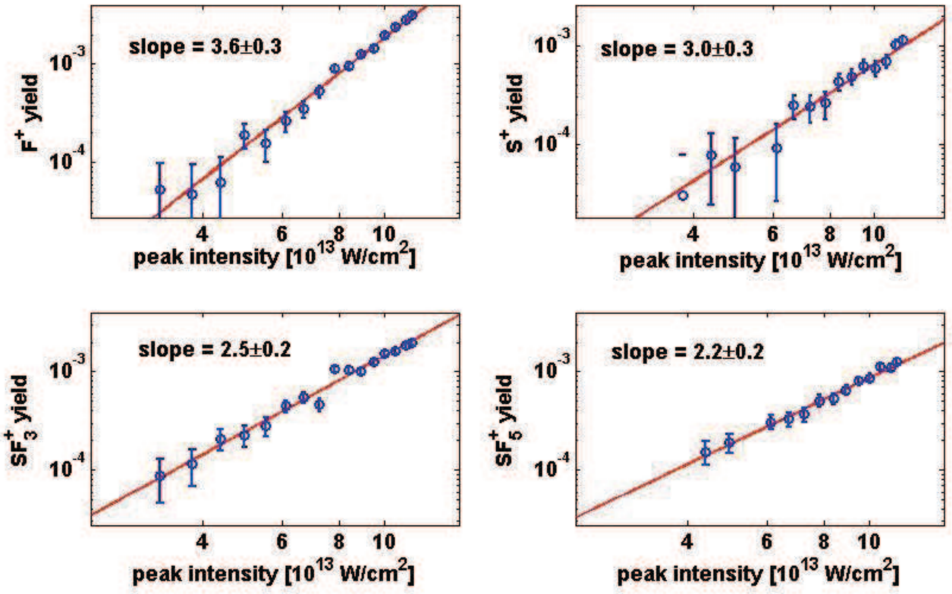

Figure 34: a log-log presentation of the power scan for some cation products. The power-law which is obtained from the slope of the linear fit should correspond to the number of photons required for the process. While the trend throughout the different products seems correct, the low values are far below expectations of the energetic processes in question.

All cationic fragments characterize by moderate slopes, ranging 2.2-3.6. The low slopes that are measured are surprising, since from **table 1** it is apparent that energy corresponding to at least ten 800nm photons is required for the ionization of SF_6 and even higher slopes would be expected for dissociative ionization to form the atomic F^+ and S^+ products. It is therefore clear that the mechanism for the formation of these cationic species cannot be assigned to a simple multi-photon process.

6.3. Ellipticity

Following the literature[100], emphasizing the role of recollision in the double ionization of neutral species, we set out to determine whether recollision is a dominant mechanism also for double detachment of an anionic system, leading to the observed highly energetic cationic products. All recollision mechanisms, in which an electron is released by the laser field, accelerated and then driven back to recollide with its parent molecule as the electric laser field oscillates in time, are extremely sensitive to the ellipticity of the laser pulse. Even an ellipticity of less than 0.2 in the laser pulse can effectively suppress processes as double ionization and high order harmonic generation by steering the electron away from its parent molecule and preventing the recollision[101]. **Figure 35** shows the single and multiple detachment yields as a function of laser ellipticity that was continuously tuned, by a quarter wave plate, from linear (ellipticity = 0) to circular polarization (ellipticity = 1). It is clear that if a recollision mechanism contributes to the multiple detachment yields its role in the process is minor. SF_6^- multiple detachment signal exhibits a gradual decrease, reaching about 70% yield for circular compared to linear polarization. In fact, a similar trend to that observed for the single detachment yield of neutral products. The gradual decrease indicates a mechanism that is different from recollision, for which a rapid drop can be predicted. It is insightful to directly compare this result to one of the background signals in our measurement which is tentatively assigned to multiple ionization and coulomb explosion of neutral molecules in the residual gas (RG). In contrast to the single and multiple detachment signals, the black line in **figure 35** shows a strong effect of ellipticity on the RG products, suggesting a recollision driven multi-ionization process. The sharp 50% drop of the RG signal, at ~0.2 ellipticity and less than 10% for circular polarization is consistent with the published results for recollision dominated processes[101].

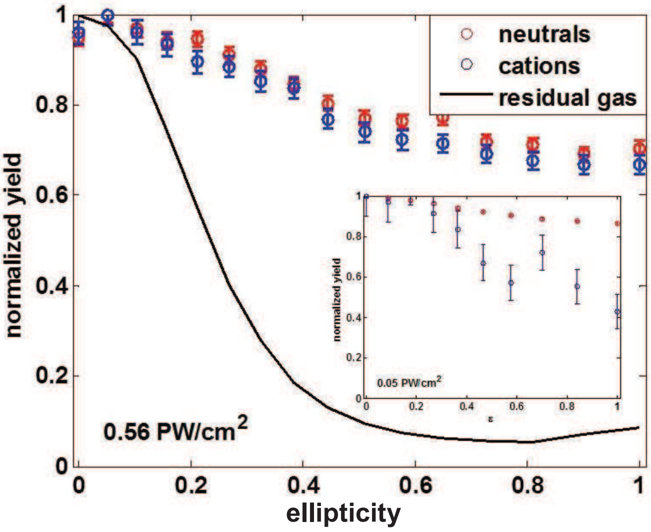

Figure 35: the results of an ellipticity scan, tuned from linear to circular polarization of the laser. Both single and multiple detachment processes show little dependence on the ellipticity (also for low intensities - insert), compared to the ionization of the residual gas, which is reasonably governed by recollision.

The measurement described was done using a focusing distance of 3mm, a region dominated by F^+ production as described above. The same scan was executed for the other regions, far focused with large fragments dominating and the intermediate region. As apparent from insert of **figure 35,** even at low intensities recollision is not a prominent mechanism for multi-detachment of SF_6^-.

Signal dependence on circular polarization may be analyzed in terms of molecular alignment. Alignment mechanisms are a common way of interpreting the differences between TOF spectra resulting from linear and circular polarization[102]. An enhanced signal at circular polarization can be naively interpreted as geometric alignment, since the rotating polarization interacts with more of the isotropic distribution of molecules, compared with linear polarization that strongly interacts only with molecules with favorable alignment. On the other hand, in dynamic alignment the molecules are assumed to be aligned by a linearly polarized pulse prior to the detachment, eliminating the advantage of circular polarization. In contrast to our data, intense field ionization measurements of neutral SF_6 molecules[98] showed an increased yield of atomic F^+ ions for circular polarization compared to linear polarization. Ren *et al* interpreted their observation as an indication that the randomly oriented neutral SF_6 molecules are not dynamically aligned by the linear laser pulse, resulting in an improved geometric alignment of the relatively symmetric molecules with the circularly polarized laser pulse. As we indicated in chapter 1 and earlier in this chapter, recent calculations[55] indicate that the additional electron in the anionic SF_6^- breaks the symmetry of the system and could possibly begin to explain the difference between the two measurements. It should be noted that for high KER products such as the F^+ products, experimental artifacts, such as dependence of detector acceptance on F^+ emission angle, may skew such measurements. In our design the absence of such artifacts was confirmed by measurement as a function of angle between the TOF axis and linearly polarized pulses without an observable change in ion yields, as was earlier claimed regarding **figure 30** for the two extreme angles.

Dependence on the polarization may also be understood through angular momentum motivated selection rules, their importance even greater in resonant multi-photon excitations. One can imagine a photo-excited electron obtaining angular momentum that to some extent depends on the field ellipticity, and the efficiency of the excitation of this electron through a resonant state will be determined by the transition dipole between the states. To further quantify the affect of alignment and transition rules, more thorough investigation must be made regarding the intensity dependence and the different dissociation channels involved.

6.4. Chirp

As the ellipticity dependence rules out the recollision mechanism, we set out to further examine the multiple detachment mechanism by modification of the laser pulse shape. Similar to spatial focusing of the laser pulse, it is possible to change the pulse length by introducing chirp. Recalling that chirp is introduced by the second order of the tailor expansion of the spectral phase, the result is a change of frequency as a function of time, effectively widening the temporal profile of the pulse. **Figure 36** shows the dependence of the yields of the different charged states on the chirp. Since all species are products of non-linear processes, their yields are bound to depend on the chirp through their dependence on the peak intensity. The widening of the pulse while the total power is kept constant reduces the peak intensity and lowers the measured product yields.

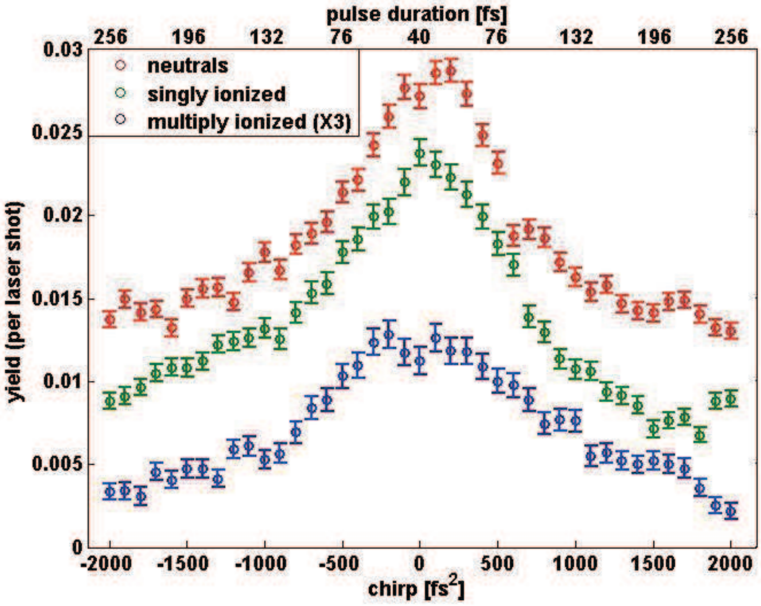

Figure 36: a chirp scan profile, demonstrating the non-linearity of the photo-detachment processes, single and multiple. The temporal defocusing of the pulse reduces the intensity (from a maximum of 0.56PW/cm^2 at this regime), to which the non-linear products are sensitive.

Although positive and negative chirps differ by the change in central wavelength from red to blue or blue to red respectively, the drop in pulse intensity is expected to be symmetric with respect to chirp sign. As can be seen in **figure 36** the photo-detachment yields follow a symmetric trend, following the peak intensity. The small a-symmetric features could very well be a due to some finite residual spectral phase in the unshaped pulses. **Figure 37** shows the mass resolved chirp dependence of the cationic species, measured at milder 0.11PW/cm^2 intensities. Even at these intensities the sensitivity to chirp shows a similarly symmetric trend for the different products. The BR of the different channels exhibits chirp dependence as shown in **figure 38**. As can be expected from the respective appearance energies of the F^+ and SF_n^+ channels, the relative fraction of the atomic F^+ yield goes down as we introduce positive or negative chirp.

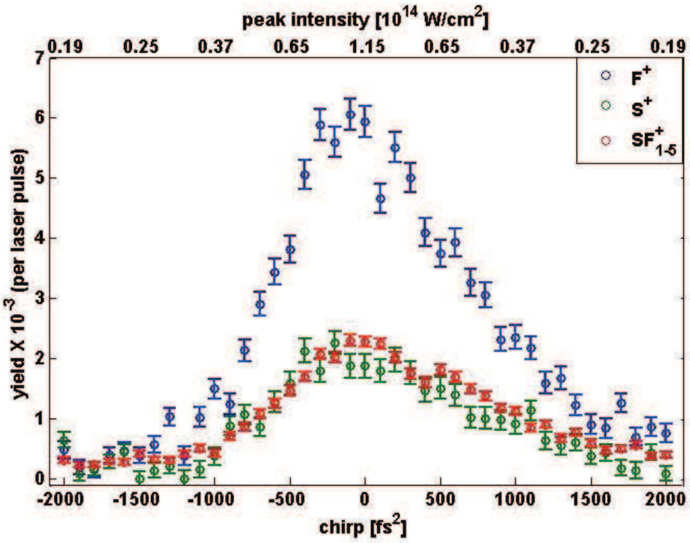

Figure 37: a chirp scan presenting the multi-detachment fragment yields, at the threshold intensities of appearance. For all ranges of appearance energies, the different fragments experience symmetric trands.

Figure 38: at moderate focusing we again see the signature of channel crossing, as the energetic F^+ product becomes dominant as the intensity is increased.

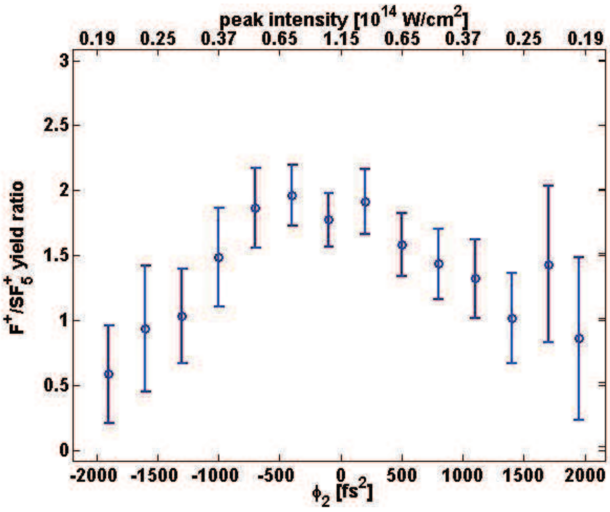

The dependence of the peak intensity on the pulse length is an important trait enabling our femto-second lasers to reach high intensities. From the temporal profile expression of a Gaussian beam $I(t) \propto \frac{P}{\tau} e^{-\frac{4ln2t^2}{\tau^2}}$ it is evident that the peak intensity increases linearly with the pulse power, and is inversely dependent on the FWHM duration of the pulse, τ. The yield of photo-detachment products of a non-linear process with a power-law n, will follow the simple scaling described in **equation 23**. We used this power-law dependence in section 6.2 to deduce the non-linear power degree by tuning the over-all power. The widening of the pulse achieved by introducing chirp reduces the peak intensity but also extends the interaction time affecting the measured yield. In **equation 24** we introduce the inverse normalized pulse duration $k = \frac{\tau_0}{\tau}$, τ_0 being the un-chirped duration, and obtain a power-law dependence of $n - 1$.

(24) $$yield = \int I(t)^n dt \propto \int \left(\frac{P}{\tau} e^{-\frac{4ln2t^2}{\tau^2}}\right)^n dt$$

$$= \frac{P^n}{\tau^n} \int e^{-\frac{n4ln2t^2}{2\tau^2}} dt$$

$$= \frac{P^n}{\tau^n} \sqrt{\frac{\pi}{4ln2n}} \tau$$

$$\rightarrow yield(k) \propto P^n \tau(k)^{1-n} = P^n {\tau_0}^{1-n} k^{n-1}$$

Figure 39 presents the results of the chirp scan at moderate intensities (equivalent of **figure 37**, to avoid saturation), as a function of the normalized pulse length k. From the log-log presentation the slope of $n - 1$ allows extraction of the process power law, n, presented in the figure for the single detachment neutral product and for two of the double detachment fragments. Here again saturation is observed at high intensities (large k), which were excluded from the fits. The results are summarized in **table 3**, and compared to the corresponding power-laws resolved by the power scan technique. The chirp scan results are in reasonable agreement with the power scan experiments, and correspond to the same discussion.

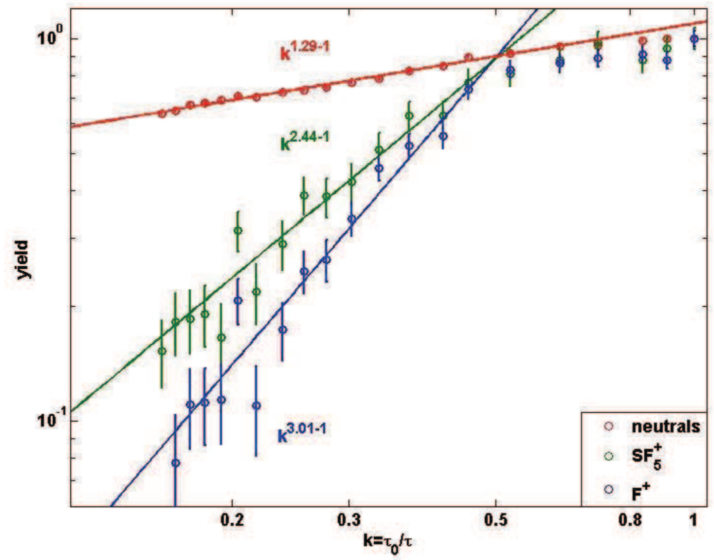

Figure 39: the chirp scan presented as a function of $k = \tau_0/\tau$, and as a result intensity reduction, of the pulse due to introducing chirp. The power-law fits k^{n-1} are equivalent to the power attenuation scans in section 6.2.

Table 3: summery of the power-law attributed for the non-linear processes generating neutrals and cation F^+ and SF_5^+ fragments. The values were obtained by two methods – power attenuation and chirp tuning.

Power-Law Meas. Product	Power scan	Chirp scan
neutrals	1.5±0.3	1.29±0.01
SF_5^+	2.2±0.2	2.44±0.18
F^+	3.6±0.3	3.01±0.27

We can further on try to decouple the intensity effect from the temporal effect, by simultaneously tuning both the chirp and attenuating the power in a complementary way. By attenuating the compressed pulses, and increasing total power with the addition of chirp we can fix the peak intensity at a constant value, $\frac{P}{\tau} = I_0$, and effectively only change the pulse duration. The power law dependence of **equation 24** becomes linear in τ (or k^{-1}). **Figure 40** shows a power-law dependence smaller than one (linear in log-log presentation with slope<1), indicating a non-trivial dependence on the temporal width of the pulse. The widening of the pulse suppresses both processes, single- and double-detachment, resulting with smaller yields at wide pulses than anticipated. It should be noted that here there isn't an effect of saturation as the peak intensity is kept constant at low intensities ($0.03 PW/cm^2$), though the peak value is at the limit of saturation.

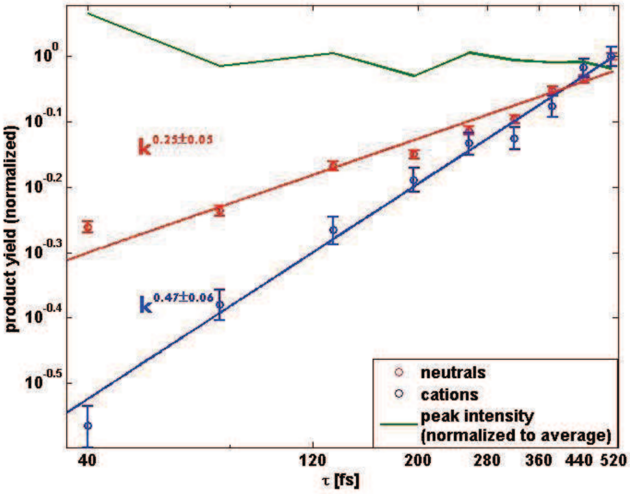

Figure 40: the effect of the pulse duration, measured by applying chirp and power attenuation in a complementary manner retaining the peak intensity throughout the scan (reaching φ_2=4000fs^2).

6.5. TOD

As the ellipticity dependence rules out the recollision mechanism, one has to consider the possibility of a sequential mechanism. In a sequential mechanism, SF_6^- would be first singly detached during the rising of the pulse and the resulting SF_6 neutral molecules will be further ionized by the peak of the pulse, resulting in a cation spectrum similar to intense ionization of neutral SF_6. In order to experimentally test this possibility we examine the dependence of the observed multiple detachment signal on asymmetrically shaped pulses that are generated by applying third order dispersion (TOD) with our pulse shaper. Introducing positive TOD will produce pulse shapes with post-pulses following a main pulse, while negative TOD will generate pre-pulses followed by the main pulse. We expected a sequential process to be enhanced by negative TOD, as the weak pre-pulses would effectively detach the loosely bound electron, preparing ample neutral SF_6 molecules to be further ionized by the main intense pulse. In contrast, for positive TOD, the weak post pulses will not be intense enough to contribute to the multiple ionization signal beyond the signal of the main intense pulse.

Results from a TOD scan do show clear a-symmetry, as can be seen in **figure 41**, but in the opposite direction! Positive TOD with post-pulses led to higher yield of multiple-detachment.

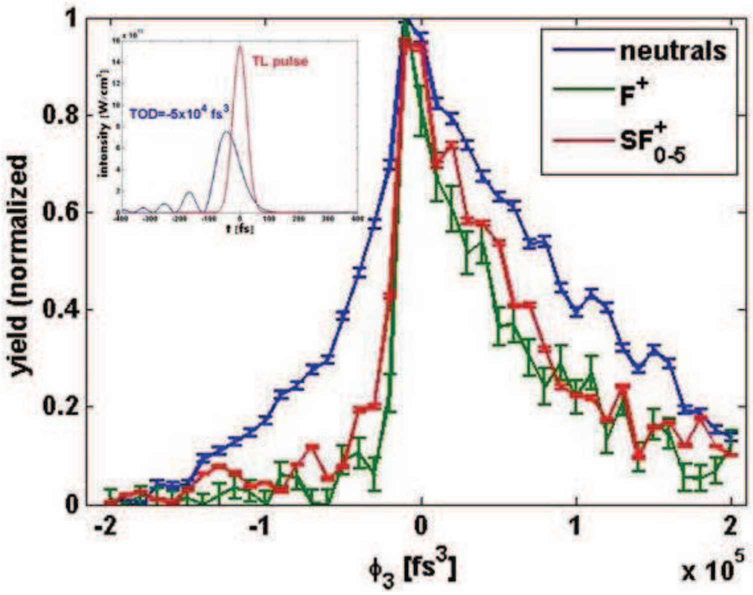

Figure 41: the TOD scan profile of the single and multiple detachment signals. A pronounced suppression of the signal is observed for negative TOD, corresponding to a pre-pulsed a-symmetry. This results in more than ten pre-pulses at the scan edges, and intensity reduced to 20%.

As introducing TOD also reduces the peak intensity of the main pulse, we wanted to estimate the peak intensity effect by comparing to the same peak intensities induced by symmetrically stretching the pulses with chirp. **Figure 42** compares the chirp and TOD scan results as a function of the computed peak intensity of the shaped pulses. While for positive TOD, product yields seem to follow the same intensity dependence as for the chirp scan, negative TOD leads to a rapid drop in cation yields. We conclude that the pre-pulses induced by negative TOD effectively suppress multiple detachment of SF_6^-. We evaluate this a-symmetry by the ratio of the average product yields with negative and positive TOD in the range of 10^4 – 10^5 fs^3. The cationic fragments exhibit high a-symmetry of 5.73±0.04 for the SF_n^+ fragments (n including 0 to 5), and F^+ yields exhibit a strong a-symmetry of 9.67±0.05. For comparison neutral yields show merely 2.01±0.01 a-symmetry that is mainly due to high KER neutrals that are most likely also due to the dissociative ionization of cations. When subtracting the high KER neutral yield, we observe a close to symmetric 1.40±0.02 trend for the narrow neutrals peak assigned to single detachment forming intact SF_6 molecules. The suppression of multiple-ionization by pre-pulses that can detach the first electron before the arrival of the intense main pulse strongly suggests that the excess weakly bound electron in SF_6^- plays an important role in the detachment of the stronger bound electrons.

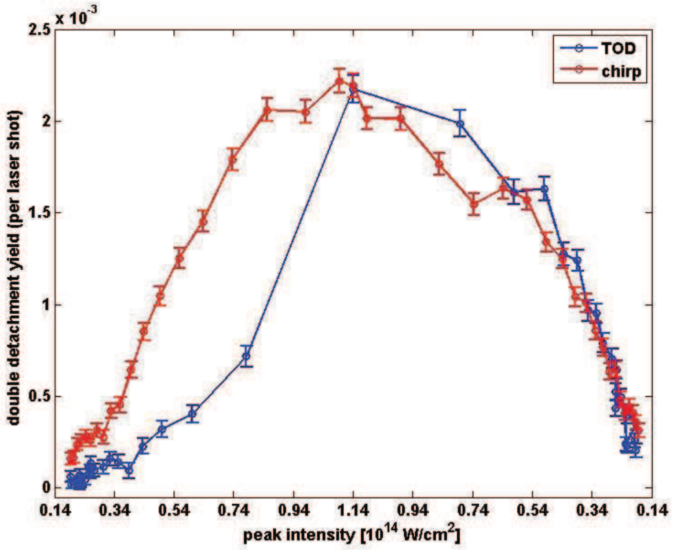

Figure 42: comparing the chirp scan with the TOD scan, in terms of the intensity reduction. This way we can evaluate the extent to which the negative TOD suppresses the signal of the different products.

We conclude that the first electron has an influence on the occurrence of the following ionizations, even if not in a direct fashion as in the recollision mechanism. We can propose several ways in which the excess electron may enhance the interaction with the intense laser field. Recent calculations indicate that the symmetric neutral SF_6 molecule is distorted by the addition of the excess electron[55]. This may imply to the existence in SF_6^- of a permanent dipole moment as opposed to SF_6, which may assist in molecular alignment leading to higher efficiencies of the photo-detachment processes. Furthermore, the loosely bound electron will increase the polarizability of the system that will in turn increase its coupling to the intense laser field. Evidence accompanied by calculations showed[103] that molecular polarizability may enhance sequential non-adiabatic excitations.

Our conclusion that the multiple-detachment mechanism requires the first loosely bound electron, is in accord also with the cation yield measured as a function of pulse length and discussed in the previous section. The sub-linear increase in cation yields observed while increasing the pulse length can be tentatively explained as suppression due to single detachment occurring early during the pulse.

7. Conclusions and outlook

In conclusion, the non-linear single and multiple detachment processes of molecular SF_6^- anions with ultrafast and intense laser pulses were observed. Neutral and cationic product yields were measured as a function of laser power, peak intensity, pulse time, polarization ellipticity and pulse shape. The measured yields of double detachment as a function of ellipticity lead us to exclude contribution from possible recollision processes – a dominant mechanism in multiple-ionization of neutral species.

On the other hand, detailed comparison of chirp and TOD pulses, showing pre-pulse suppression of multiple detachment processes, leads us to conclude that the excess electron in SF_6^- is not merely a spectator, but plays a crucial role in SF_6^- multiple-detachment. The successive processes of single detachment and further ionization of SF_6^- are apparently dependent of the temporal profile of the laser pulse, as observed through the chirp scans. This time dependence further demonstrates the influence the liberated electron has on the ionization of the molecule.

Other explanations of the time dependence may be related to nuclear wave-packet dynamics on the neutral SF_6 state leading to change in Franck-Condon overlap with resonances that may participate in the multiple ionization. However, one would expect such dynamics to also be sensitive to the sign of pulse chirp, which is not observed in our data.

Further studies on the SF_6^- system, modified by attachment of an additional atom or molecule, e.g. $Ar\cdot SF_6^-$, $H_2O\cdot SF_6^-$ or $(SF_6)_2^-$, will help to further investigate the intense laser interaction with molecular systems of increasing complexity. Presently, studies of SF_6^- using coincidence imaging techniques, as well as pump-probe studies are pursued, and will further expand our understanding of multiple-detachment and dissociation dynamics of molecular anions with intense laser pulses.

Appendix A – the Keldysh parameter

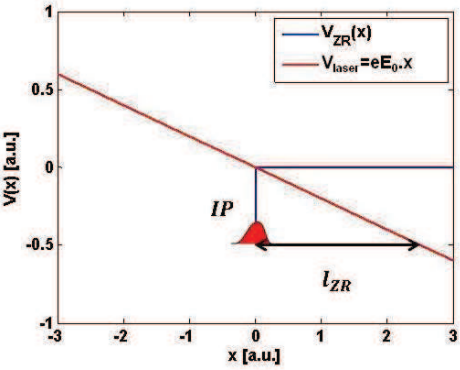

Figure 43: an illustration of the simplistic zero-range potential.

As described in chapter 1, the tunneling ionization (TI) channel is plausible when its rate is higher than the laser frequency, thus allowing tunneling before the force changes direction. In this regime, which may be achieved by increasing the laser intensity as described below, the TI picture is more appreciable for describing ionization rather than the multi-photon (MPI) channel. The tunneling time, t_{tunn}, corresponds to a tunneling length, l_{tunn}, dependent on the electronic system involved through the ionization potential, and on the laser through the field strength. A simple connection can be derived assuming a Zero-Range potential, illustrated in **figure 43**:

(25)

$$\left.\begin{array}{l} slope = eE_0 \\ slope = \frac{IP}{l_{ZR}} \end{array}\right\} \rightarrow l_{ZR} = \frac{IP}{eE_0}$$

The time is then calculated using the electron average velocity, which is in turn, defined using the Varial Theorem:

(26)

$$\frac{1}{2}m_e < v >^2 = < T > \overset{VT}{=} IP \rightarrow < v > = \sqrt{\frac{2IP}{m_e}}$$

From **equations 25-26** the Keldysh parameter could be derived as a function of intensity:

(27)

$$\gamma = \frac{t_{tunn}}{\frac{t_0}{2}}$$

$$= \frac{2\omega_0}{\omega_{tunn}}$$

$$= \omega_0 \frac{\sqrt{2 \cdot IP \cdot m_e}}{eE_0}$$

$$= \frac{2\pi c}{e\lambda} \sqrt{c\varepsilon_0 n m_e} \cdot \sqrt{\frac{IP}{I_0}}$$

$$\sim 5 \cdot 10^6{}_{\sqrt{W}/cm} {I_0}^{-1/2}$$

While c is the velocity of light, ε_0 the vacuum permittivity, e the electrons charge and experimental properties were used: $\lambda = 800nm; IP = 3eV$ as well as the field-intensity relation $E_0 = \sqrt{\frac{2I_0}{\varepsilon_0 \cdot n \cdot c}}$.

If the tunneling rate exceeds the laser frequency, tunneling occurs preferentially, and $\gamma < 1$ corresponding to intensities on the order of $10^{13} W/cm^2$ and higher.

Appendix B – the residual gas

Like all experimental vacuum systems we don't achieve total vacuum. Utilizing a baking setup we reach pressures as low as $1 \cdot 10^{-9}$ Torr. We can approximate the number of residual gas particles subjected to the intense laser beam to understand the magnitude of our noise. If we assume an interaction volume, V_{int}, combined of the average laser width along the length of the interaction zone, and assume a low temperature of a few tens of ^{o}K, we can calculate this quantity:

(28) $$N = \frac{P}{kT} V_{int} = \frac{1 \cdot 10^{-9} Torr}{kT} 5mm \cdot \pi \cdot (50\mu m)^2 \cong 10^5 particules$$

We can further distinguish the components of this gas by looking at its spectrum (for instance by lasing into the vacuum system without activating the Pulsed valve). We need to calibrate to mass, remembering that the calibration for these molecules is different than for the SF$_6$ species, since their TOF starts from the spectrometer (length L to detector), and they are accelerated by one part of the spectrometer alone (V). **Figure 44** shows a residual gas spectrum, with the appropriate TOF from the interaction zone. A simple calculation reveals we have mostly water and hydrogen:

$$TOF = \frac{L}{v} = \frac{L}{\sqrt{\frac{2eV}{m}}} \rightarrow m = TOF^2 \frac{2eV}{L} \begin{cases} 1^2 \frac{2e1.8kV}{0.6m} \sim 1amu \\ 4.5^2 \frac{2e1.8kV}{0.6m} \sim 18amu \end{cases}$$

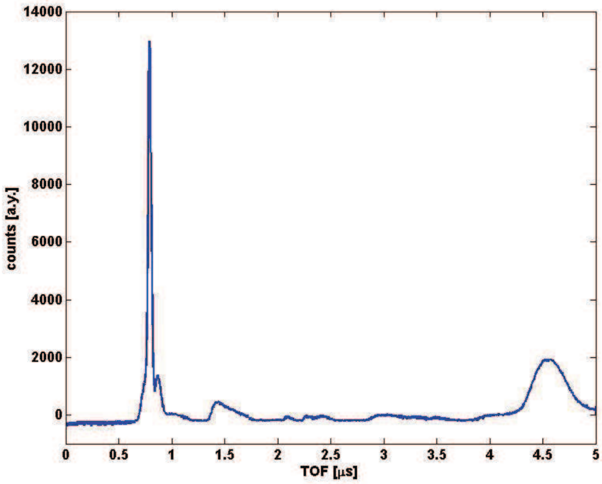

Figure 44: residual gas TOF spectrum, indicating presence of mainly water and hydrogen in our 10^{-9} Torr vacuum chamber.

Appendix C – detector acceptance

As mentioned in the text, we applied a 1.8kV to the spectrometer, for mass over charge distinguishing between the different photo-detachment products. A second independent a-symmetric voltage of 2.5kV was applied to the electrode adjacent to the interaction zone, to prevent the spectrum noise caused by ionized residual gas. The choice of these voltages was empiric, though they coincide with calculations, and was found to balance between the necessity to suppress noise and the need for sufficient impact energy to meet the acceptance conditions of the detector.

To evaluate the impact energy required for detection we measured the yield of the small fluorine cation, while tuning the spectrometer voltage, as presented in **figure 42**. The constant a-symmetric voltage we used, 2.5kV, was found to best repel the residual gas, and the main spectrometer voltage was sought accordingly. The top axis of **figure 42** shows calculation results of the F^+ energy corresponding to the different applied spectrometer voltage, keeping in mind that the cation fragments carry only a fraction of the original energy of the molecule, in proportion to their mass. Thus, the smallest cation, the Fluorine ion, carries only about 13% of the energy produced by the 5kV accelerator and the first part of the spectrometer. Calculations show that for detection of the F^+ a voltage of 1.2kV is required from the spectrometer, corresponding to 2kV carried by the fragment.

On the other hand, there is a limit to the efficiency of increasing the voltage, after which the spectrometer is saturated. From **figure 45** it is clear we do not benefit in detection at voltages higher than 1.8kV, on the contrary, the efficiency at repelling the residual gas is hindered at higher voltages leading to a noisy spectrum. For comparison the neutralized SF_6 yield is also presented, its efficiency and saturation occurring at lower voltages.

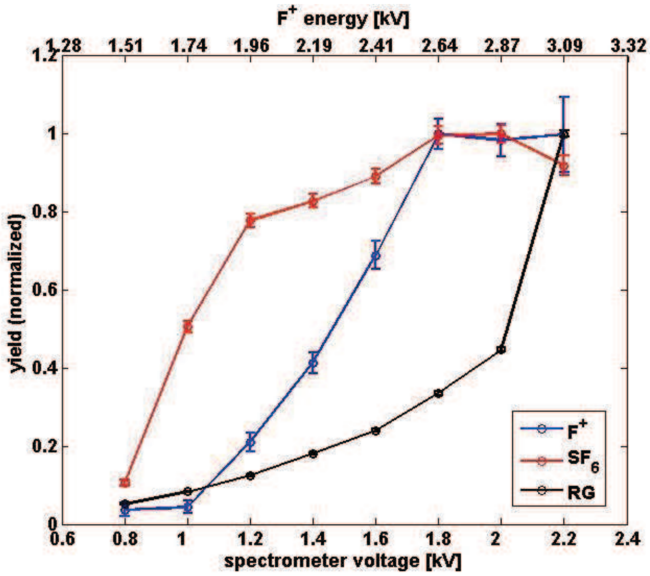

Figure 45: detector efficiency measurement. For the F^+ ion both limits of efficiency are noticed: a minimal voltage of 1.2kV, corresponding to 2kV impact energy, and a saturation limit of 1.8kV corresponding to 2.5kV F^+ energy. Besides saturation, increasing the voltage brings to higher noise signal. The neutral signal is assumed to be effected by the neutral fragments.

It should be pointed out that this efficiency profile is appropriate specifically for the cation products. It reflects an efficient detection regime of 2-2.5kV of energy for a detected particle, but it takes into account the spectrometer voltage setup as described above with the a-symmetric electrode used to deflect the residual gas cations. This electrode serves as a barrier also for the small cations which remain with a small fraction of the parent molecule initial energy. Thus a larger voltage is required for the spectrometer, in order to give them sufficient energy for detection. This is not true for the neutral fragments, which are un-affected by this barrier, and are efficiently detected with energies lower then 1kV, as was demonstrated by preliminary coincidence measurements. Accordingly, we attribute the large decline in the neutral yield not to SF_6, which carries over 5kV for the whole range of voltages. Rather we attribute this trend to neutral fragments, mainly F, products of the SF_6^+ fragmentation. From this we calculate that as little as 0.5kV carried by the smallest fragment, is enough for detection without the a-symmetric electrode, which doesn't affect neutral particles (**figure 46**).

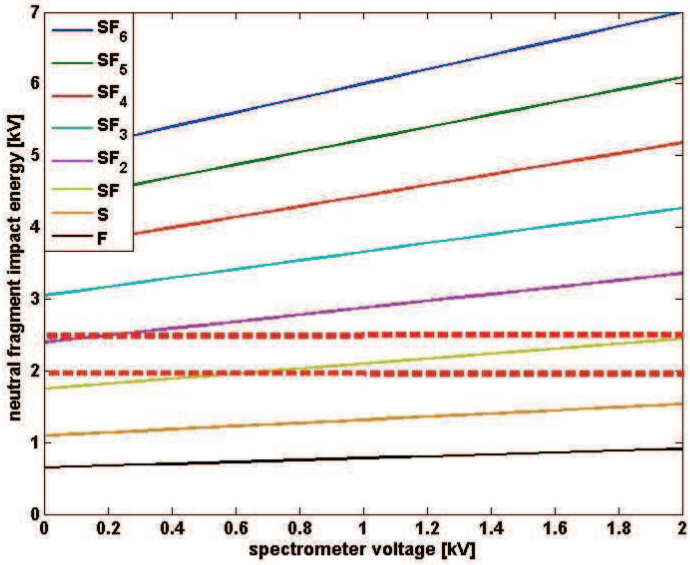

Figure 46: calculation results of neutral fragment energies corresponding to different spectrometer voltages. Dashed red lines reflect the cation detection regime, affected by the a-symetric barrier. The neutral fragments are un-affected and are detected throughout the range of voltages.

Appendix D – data acquisition and analysis

The signals we measure in our experiments are in the form of the times at which the particles hit the MCP, indicating their Time of Flight (TOF) from a certain reference time. We measure from the time at which the accelerator electrodes are turned on, as described in the text. The recording of these times involve a few techniques of data acquisition to be described in this appendix. Furthermore, the cleaning of the data, and the way we deal with noise will be discussed.

The MCP is an electron multiplier, generating electrons when particles have impact with the MCP electrode that cascade through micrometer channels to produce a measurable current. This current is measured in means of voltage, and in our setup can also be recognized spatially by a Sulfuric plate at the end of the MCP.

The voltage pulse is transmitted to a Constant Fraction Discriminator (CFD). The objective of this device is finding the maximum of the signal, and using it to trigger a counter and turn the voltage to a time stamp. Unlike threshold triggering which is peak-height dependent, using a CFD the triggering is on a constant fraction of the peak, and therefore trigger times are height independent.

The CFD is to be followed by a Time to Digital Converter (TDC), through a module (NIM) enabling the logic translation to time-stamps recorded by the TDC. The time-stamps are converted to digital representation recognized by the computer program and recorded.

These TOF include noise; other gaseous molecules ionized by the laser and accelerated by the spectrometer. These residual gas molecules arrive at TOF similar to the SF_6^- products and severe our ability to resolve the spectrum. In addition the parent ion itself may produce a wide signal overlapping its products spectrum. In order to diminish this background, we carry out a technique of measuring a background measurement with the laser delayed by $40\mu s$ (**figure 47** row **(2))**. This provides us with spectrums of both ion background (presented in **(A2)**), and laser background (**(B2)** – **(B1)** taking into account the original noise at the second half of the spectrum). The clean signal is obtained by the subtraction presented in the figure.

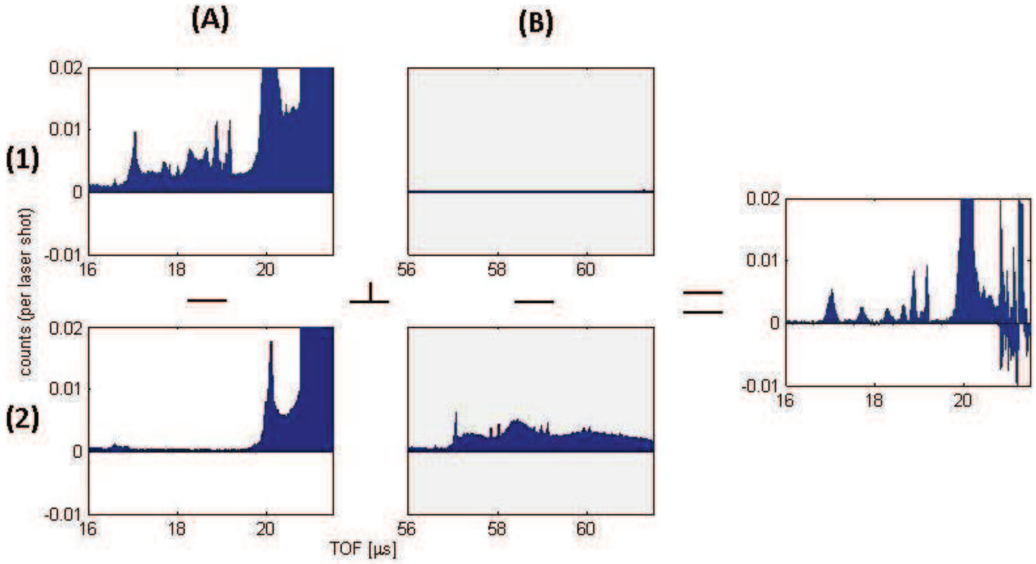

Figure 47: subtraction technique using two alternating measurements of the TOF spectrum. One is with the laser synchronized with the ion-beam (top), and the second times the laser $40\mu s$ later (bottom) enabling subtraction of the ion background. Analysis of the $40\mu s$-later spectrum enables further subtraction of the laser background to yield the clean product spectrum (right).

References

---

[1] P. F. McManamon, "Review of ladar: a historic, yet emerging, sensor technology with rich phenomenology," Optical Engineering, vol. 51, no. 6, 2012.

[2] F. Helmchen and W. Denk, “Deep tissue two-photon microscopy,” Nature methods, 2005.

[3] P. Campagnola and L. Loew, “Second-harmonic imaging microscopy for visualizing biomolecular arrays in cells, tissues and organisms,” Nature biotechnology, 2003.

[4] J. Cheng and X. Xie, “Coherent anti-Stokes Raman scattering microscopy: instrumentation, theory, and applications,” The Journal of Physical Chemistry B, 2004.

[5] C. Freudiger, W. Min, B. Saar, S. Lu, and G. Holtom, “Label-free biomedical imaging with high sensitivity by stimulated Raman scattering microscopy,” Science, 2008.

[6] T. Ye, D. Fu, and W. Warren, “Nonlinear Absorption Microscopy,” Photochemistry and photobiology, 2009.

[7] A. Zewail, “Femtochemistry: Atomic-scale dynamics of the chemical bond,” The Journal of Physical Chemistry A, vol. 104, pp. 5660–5694, 2000.

[8] A. Stolow, A. E. Bragg, and D. M. Neumark, “Femtosecond time-resolved photoelectron spectroscopy.,” Chemical reviews, vol. 104, no. 4, pp. 1719–57, 2004.

[9] F. Krausz and M. Ivanov, “Attosecond physics,” Reviews of Modern Physics, vol. 81, 2009.

[10] G. M. Manus and C. Mainfray, “Multiphoton ionization of atoms,” Reports on Progress in Physics, vol. 54, pp. 1333–1372, 1991.

[11] R. W. Boyd ,Nonlinear Optics, 2007.

[12] T. Brixner, T. Pfeifer, G. Gerber, M. Wollenhaupt, and T. Baumert, Femtosecond Laser Spectroscopy, 2005

[13] K. Walowicz, I. Pastirk, V. V Lozovoy, and M. Dantus, “Multiphoton intrapulse interference. 1. Control of multiphoton processes in condensed phases,” The Journal of Physical Chemistry A, vol. 106, no. 41, 2002.

[14] R. J. Levis, G. M. Menkir, and H. Rabitz, “Selective bond dissociation and rearrangement with optimally tailored, strong-field laser pulses.,” Science (New York, N.Y.), vol. 292, no. 5517. pp. 709–13, 2001.

[15] P. Bustard, G. Wu, and R. Lausten, “From molecular control to quantum technology with the dynamic Stark effect,” Faraday discussion, vol. 153, pp. 321–342, 2011.

[16] P. Bucksbaum, A Zavriyev, H. Muller, and D. Schumacher, “Softening of the H_2^+ molecular bond in intense laser fields.,” Physical review letters, vol. 64, no. 16. pp. 1883–1886, 16-Apr-1990.

[17] B. Sheehy and L. DiMauro, “Atomic and molecular dynamics in intense optical fields 1,” Annual review of physical chemistry, 1996.

[18] J. Posthumus, “The dynamics of small molecules in intense laser fields,” Reports on Progress in Physics, vol. 67, pp. 623–665, 2004.

[19] P. Agostini, F. Fabre, G. Mainfray, G. Petite, N. Rahman, "Free-Free Transitions Following Six-Photon Ionization of Xenon Atoms", Physical Review Letters, vol. 42 no. 17, 1979.

[20] K. Sattler, J. Mühlbach, O. Echt, P. Pfau, and E. Recknagel, “Evidence for Coulomb explosion of doubly charged microclusters,” Physical Review Letters, vol. 47, no. 3, 1981.

[21] T. Fennel *et-al*, “Laser-driven nonlinear cluster dynamics,” reviews of modern physics, vol. 82, 2010.

[22] J. Eden, “High-order harmonic generation and other intense optical field-matter interactions: Review of recent experimental and theoretical advances,” Progress in Quantum Electronics, vol. 28, 2004.

[23] P. Corkum, “Plasma perspective on strong field multiphoton ionization,” Physical Review Letters, vol. 71, no. 13, pp. 1994–1997, 1993.

[24] P. Corkum and F. Krausz, “Attosecond science,” Nature Physics, 2007.

---

[25] J. Itatani *et al*, “Tomographic imaging of molecular orbitals.,” Nature, vol. 432, no. 7019. pp. 867–71, 2004.

[26] C. Guo, M. Li, J. Nibarger, and G. Gibson, “Single and double ionization of diatomic molecules in strong laser fields,” Physical Review A, vol. 58, no. 6, pp. R4271–R4274, 1998.

[27] A. E. Boguslavskiy *et al*, “The multielectron ionization dynamics underlying attosecond strong-field spectroscopies.,” Science, vol. 335, no. 6074, pp. 1336–40, 2012.

[28] V. S. Prabhudesai, U. Lev, A. Natan, B. D. Bruner, A. Diner, O. Heber, D. Strasser, D. Schwalm, I. Ben-Itzhak, J. J. Hua, B. D. Esry, Y. Silberberg, and D. Zajfman, “Tracing the photodissociation probability of H_2^+ in intense fields using chirped laser pulses,” Physical Review A, vol. 81, no. 2, p. 023401, 2010.

[29] M. Zohrabi *et al*, “Vibrationally resolved structure in O_2^+ dissociation induced by intense ultrashort laser pulses,” Physical Review A, vol. 83, no. 5, p. 053405, 2011.

[30] J. McKenna *et al*, “Benchmark Measurements of H_3^+ Nonlinear Dynamics in Intense Ultrashort Laser Pulses,” Physical Review Letters, vol. 103, no. 10, p. 103004, 2009.

[31] J. Greenwood, “Double ionization of atomic negative ions in an intense laser field,” Journal of Physics B Atomic Molecular and Optical Physics, vol. 36, 2003.

[32] J. Pedregosa-Gutierrez *et al*, “Evidence for Rescattering in Intense, Femtosecond Laser Interactions with a Negative Ion,” Physical Review Letters, vol. 93, no. 22, p. 223001, 2004.

[33] R. Reichle, H. Helm, and I. Kiyan, “Detailed comparison of theory and experiment of strong-field photodetachment of the negative hydrogen ion,” Physical Review A, vol. 68, no. 6, p. 063404, 2003.

[34] B. Bergues and I. Kiyan, “Two-Electron Photodetachment of Negative Ions in a Strong Laser Field,” Physical Review Letters, vol. 100, no. 14, p. 143004, 2008.

[35] A. Gazibegović-Busuladžić *et al*, “Electron Rescattering in Above-Threshold Photodetachment of Negative Ions,” Physical Review Letters, vol. 104, no. 10, p. 103004, 2010.

[36] I. Last and J. Jortner, “Theoretical study of multielectron dissociative ionization of diatomic molecules and clusters in a strong laser field,” vol. 58, no. 5, pp. 3826–3835, 1998.

[37] V. H. Dibeler and F. Mohler, “Dissociation of SF_6 , CF_4 , and SiF_4 by Electron Impact,” National Bareau of Standards, vol. 40, 1948.

[38] A. Hitchcock and M. Van der Wiel, “Absolute oscillator strengths (5-63 eV) for photoabsorption and ionic fragmentation of SF_6,” Journal of Physics B: Atomic Molecular and Optical Physics, vol. 12, no. 13, 1979.

[39] H. Tachikawa, “The ionization dynamics of SF_6: a full dimensional direct ab initio dynamics study,” Journal of Physics B Atomic Molecular and Optical Physics, vol. 33, pp. 1725–1733, 2000.

[40] A. Viggiano, T. M. Miller, J. F. Friedman, and J. Troe, “Low-energy electron attachment to SF_6. III. From thermal detachment to the electron affinity of SF_6.,” The Journal of chemical physics, vol. 127, no. 24, p. 244305, 2007.

[41] J. Sanderson *et-al*, “Multielectron-dissociative-ionization of SF_6 by intense femtosecond laser pulses,” Journal of Physics B: Atomic, Molecular and Optical Physics, vol. 30, 1997.

[42] J. Troe, T. M. Miller, and A. Viggiano, “On the accuracy of thermionic electron emission models. I. Electron detachment from SF_6^-,” The Journal of chemical physics, vol. 130, no. 24, p. 244303, 2009.

[43] J. C. Bopp *et al*, “Spectroscopic characterization of the isolated SF_6^- and $C_4F_8^-$ anions: observation of very long harmonic progressions in symmetric deformation modes upon photodetachment,” The journal of physical chemistry. A, vol. 111, no. 7, pp. 1214–21, 2007.

[44] A. Jalbout, A. De Leon, L. Adamaowicz, and B. Trzaskowski, “Theoretical, Empirical and Experimental electron affinities of SF_6: Solving the density functional enigma,” Journal of Theoretical and Computational Chemistry, vol. 6, no. 4, pp. 747–759, 2007.

---

[45] W. Johnstone and W. Newell, “Absolute elastic differential cross sections for electron scattering from SF_6,” Journal of Physics B Atomic Molecular and Optical Physics, vol. 473, pp. 437–487, 1999.

[46] M. B. Roque *et al*, “Production of fluorine $^{2,4}P \rightarrow {}^2P^0$ resonance radiation by electron impact on SF_6, CF_4, NF_3, and CCl_2F_2,” The Journal of Chemical Physics, vol. 94, no. 1, p. 341, 1991.

[47] A. R. Ravishankara, S. Solomon, a a Turnipseed, and R. F. Warren, “Atmospheric lifetimes of long-lived halogenated species,” Science, vol. 259, no. 5092, pp. 194–9, 1993.

[48] M. Sasanuma and E. Ishiguro, “Photoionisation of SF_6 in the XUV region,” Journal of Physics B: Atomic Molecular and Optical Physics, vol. 12, 1979.

[49] J. Troe, T. M. Miller, and A. Viggiano, “Low-energy electron attachment to SF_6. II. Temperature and pressure dependences of dissociative attachment.,” The Journal of chemical physics, vol. 127, no. 24, p. 244304, 2007.

[50] L. Gutsev and R. Barlett, “Adiabatic electron affinities of PF_5 and SF_6: a coupled-cluster study,” Molecular Physics, vol. 94, pp. 3–7, 1998.

[51] P. Datskos, J. Carter, and L. Christophorou, “Photodetachment of SF_6^-,” Chemical physics letters, vol. 239, pp. 38–43, 1995.

[52] J. Troe, T. Miller, and A. Viggiano, “Communication: Revised electron affinity of SF_6 from kinetic data,” The Journal of Chemical Physics, vol. 136, p. 121102, 2012.

[53] P. J. Hay, “The relative energies of SF_6^- and SF_6 as a function of geometry,” The Journal of Chemical Physics, vol. 76, no. 1, p. 502, 1982.

[54] P. S. Drzaic and J. I. Brauman, “Electron Photodetachment Study of Sulfur Hexafluoride Anion: Comments on the Structure of SF_6^-,” J. Am. Chem. Soc., vol. 104, pp. 13–19, 1982.

[55] W. Eisfeld, “Highly accurate determination of the electron affinity of SF_6 and analysis of structure and photodetachment spectrum of SF_6-.$^-$,” The Journal of chemical physics, vol. 134, no. 5, p. 054303, 2011.

[56] A. Hitchcock, C. Brion, and M. Van der Wiel, “Ionic fragmentation of SF_6 ionised in the sulphur 2p shell,” Journal of Physics B: Atomic Molecular and Optical Physics, vol. 11, no. 18, 1978.

[57] A. Monmayrant, S. Weber, and B. Chatel, “A newcomer’s guide to ultrashort pulse shaping and characterization,” Journal of Physics B: Atomic, Molecular and Optical Physics, vol. 43, no. 10, p. 103001, 2010.

[58] *In German*: Annalen der Physik 17 (6): 132–148 *and later translated to English as* "On a Heuristic Point of View about the Creation and Conversion of Light".

[59] P. Johnson, “Molecular multiphoton ionization spectroscopy,” Accounts of Chemical Research, vol. 13, pp. 20–26, 1980.

[60] J. Parker, C.W. Clark, "Study of a plane-wave final-state theory of above-threshold ionization and harmonic generation," Journal of the Optical Society of America B, vol. 13, no. 2 p. 371, 1996.

[61] L.V. Keldysh, " Ionization in field of a strong electromagnetic wave," Soviet Physics JETP-USSR , vol. 20, 1965.

[62] W. Griffiths and F. Harris, “Single and double ionization energies of sulphur hexafluoride measured by double charge transfer spectroscopy”, International journal of mass spectrometry and ion processes, vol. 85, pp. 259–264, 1988.

[63] R. Feifel, J. H. D. Eland, L. Storchi, and F. Tarantelli, “Complete valence double photoionization of SF_6,” The Journal of chemical physics, vol. 122, no. 14. p. 144309, 2005.

[64] A. l’Huillier, L. Lompre, G. Mainfray, and C. Manus, “Multiply charged ions induced by multiphoton absorption in rare gases at 0.53 um,” Physical Review A, vol. 27, no. 5, 1983.

[65] B. Walker, E. Mevel, B. Yang, and P. Breger, “Double ionization in the perturbative and tunneling regimes,” Physical Review A, vol. 48, no. 2, pp. 894–897, 1993.

---

[66] A. Rudenko *et al*, “Correlated Multielectron Dynamics in Ultrafast Laser Pulse Interactions with Atoms,” Physical Review Letters, vol. 93, no. 25, p. 253001, 2004.

[67] A. l’Huillier, L. Lompre, G. Mainfray, and C. Manus, “Multiply charged ions formed by multiphoton absorption processes in the continuum,” Physical Review Letters, vol. 48, no. 26, 1982.

[68] Especially for the rare gasses, cf. ref. 64-66, and ref. within for other molecules.

[69] J. Seres *et al*, “Source of coherent kiloelectronvolt X-rays,” Nature, vol. 433, 2005.

[70] P. Dietrich, N. H. Burnett, M. Ivanov, and P. B. Corkum, “High-harmonic generation and correlated two-electron multiphoton ionization with elliptically polarized light,” Physical Review A, vol. 50, no. 5, pp. 3585–3588, 1994.

[71] G. Gillen, M. Walker, and L. Van Woerkom, “Enhanced double ionization with circularly polarized light,” Physical Review A, vol. 64, no. 4, p. 043413, 2001.

[72] T. Weber *et-al*, “Recoil-ion momentum distributions for single and double ionization of helium in strong laser fields,” Physical Review Letters, vol. 843, 2000.

[73] D. Fittinghoff *et-al*, “Observation of nonsequential double ionization of helium with optical tunneling,” Physical Review Letters, vol. 69, no. 18, 1992.

[74] V. Bhardwaj *et -al*, “Few Cycle Dynamics of Multiphoton Double Ionization,” Physical Review Letters, vol. 86, no. 16, pp. 3522–3525, 2001.

[75] J. Laskin and C. Lifshitz, “Kinetic energy release distributions in mass spectrometry,” Journal of mass spectrometry, vol. 36, no. 5, pp. 459–78, 2001.

[76] Z. Vager, R. Naaman, and E. P. Kanter, “Coulomb explosion imaging of small molecules,” Science, vol. 244, no. 4903. pp. 426–31, 1989.

[77] F. Légaré *et al*, “Laser Coulomb explosion imaging for probing ultra-fast molecular dynamics,” Journal of Physics B: Atomic, Molecular and Optical Physics, vol. 39, no. 13, pp. S503–S513, Jul. 2006.

[78] http://www.newport.com/mai-tai-one-box-tunable-ultrafast-lasers/368124/1033/info.aspx

[79] http://www.newport.com/images/webDocuments-EN/images/11815.pdf

[80] K. Luria, N. Lavie, and U. Even, “Dielectric barrier discharge source for supersonic beams,” The Review of scientific instruments, vol. 80, no. 10. p. 104102, 2009.

[81] U. Even *et-al*, “Cooling of large molecules below 1 K and He clusters formation,” The Journal of Chemical Physics, vol. 112, no. 18, p. 8068, 2000.

[82] W. C. Wiley and I. H. McLaren, “Time-of-Flight Mass Spectrometer with Improved Resolution,” Review of Scientific Instruments, vol. 26, no. 12, p. 1150, 1955.

[83] SIMION® is an industry, standard charged particle optics simulation software. It solves the Laplace equations of a defined electric setup, and simulates the dynamics of particles in such a setup.

[84] C. Ellert and P. Corkum, “Disentangling molecular alignment and enhanced ionization in intense laser fields,” Physical Review A, vol. 59, no. 5, pp. R3170–R3173, 1999.

[85] J. Posthumus and J. Plumridge, “Dynamic and geometric laser-induced alignment of molecules in intense laser fields,” Journal of Physics B Atomic Molecular and Optical Physics, vol. 553, 1998.

[86] H. Wu *et al*, “Dynamic and geometric alignment of molecules induced by intense laser fields,” Optik - International Journal for Light and Electron Optics, vol. 119, no. 16, pp. 777–782, 2008.

[87] D. Normand, L. A. Lompre, and C. Cornaggia, “Laser-induced molecular alignment probed by a double-pulse experiment,” Journal of Physics B Atomic Molecular and Optical Physics, vol. 25, no. 20, pp. L497–L503, 1992.

[88] http://www.biophotonicsolutions.com/MIIPSBox640.php

[89] Femtosecond pulse shaping using spatial light modulators A. M. Weiner; Review of Scientific Instruments vol. 71, no. 5, 2000

[90] http://www.newport.com/Empower-Pulsed-Green-Lasers/501374/1033/info.aspx

---

[91] A. E. Siegman and S. W. Townsend, “Output Beam Propagation and Beam Quality from a Multimode Stable-cavity Laser,” IEEE JOURNAL OF QUANTUM ELECTRONICS, vol. 29, no. 4, pp. 1212–1217, 1993.

[92] ISO Standard 11146, “Lasers and laser-related equipment – Test methods for laser beam widths, divergence angles and beam propagation ratios”, 2005.

[93] W. Griffiths and F. Harris, “Evidence of Stable H_2O^- Ions (lifetime > 4 μsec) Formed by Charge Inversion Reactions within a Double Focusing Mass Spectrometer,” organic mass spectrometry, vol. 22, 1987.

[94] http://www.newport.com/Parallel-Windows/141051/1033/info.aspx#tab_Specifications

[95] V. V Lozovoy, I. Pastirk, and M. Dantus, “Multiphoton intrapulse interference. IV. Ultrashort laser pulse spectral phase characterization and compensation,” Optics letters, vol. 29, no. 7, pp. 775–7, 2004.

[96] *For example*: J. Sanderson *et-al*, “Multielectron-dissociative-ionization of SF6 by intense femtosecond laser pulses,” Journal of Physics B: Atomic, Molecular and Optical Physics, vol. 30, 1997.

[97] Ref. 56; *c.f.* V. Dibeler and J. Walker, “Photoionization Efficiency Curve for SF in the Wavelength Region 1050 to 600 Å,” The Journal of Chemical Physics, vol. 44, no. 12, 1966.

[98] H. Ren, R. Ma, X. Li, J. Chen, H. Yang, and Q. Gong, “Multielectron dissociative ionization of SF6 in an intense femtosecond laser field,” International Journal of Mass Spectrometry, vol. 235, no. 2, pp. 117–122, 2004. *Compare to* ref. 96

[99] *Compare*: M. Cervenan and N. Isenor, “Multiphoton ionization yield curves for gaussian laser beams,” Optics Communications, vol. 13, no. 2, pp. 175–178, 1975. *and*: S. Hankin, D. Villeneuve, P. Corkum, and D. Rayner, “Nonlinear ionization of organic molecules in high intensity laser fields,” Physical review letters, vol. 84, no. 22, pp. 5082–5, 2000.

[100] *e.g.* ref. 66, 101.

[101] G. Gillen, M. Walker, and L. Van Woerkom, “Enhanced double ionization with circularly polarized light,” Physical Review A, vol. 64, no. 4, p. 043413, 2001.

[102] *Ref.* 84,86, *c.f. ref.* 85 *and* S.Banerjee, G.R.Kumar, D.Mathur, "Dynamic and geometric alignment of CS_2 in intense laser fields of picosecond and femtosecond duration," Physical Review A, vol. 60, 1999.

[103] A. N. Markevitch *et al*, “Sequential nonadiabatic excitation of large molecules and ions driven by strong laser fields,” Physical Review A, vol. 69, no. 1, p. 013401, 2004.

The Hebrew University of Jerusalem האוניברסיטה העברית בירושלים

הפקולטה למתמטיקה ולמדעי הטבע
המכון לכימיה

אינטראקציות של לייזר עוצמתי עם מולקולות אניוניות

הבנת תהליך תלישת אלקטרונים באניון ה–SF_6^-

עבודת מחקר לשם קבלת תואר מוסמך
בכימיה פיזיקלית

ישי אלבק

ת.ז. 02176112-7

מנחה: ד"ר דניאל סטראסר

ניסן תשעג

"אתה חוען לאדם דעת ומלמד לאנוש בינה" (מתוך התפילה)

תקציר

אינטראקציה של פולסי לייזר עוצמתיים עם חומר כגון מולקולות או קבוצות קטנות, מציגה עושר של תופעות הרגישות לא רק לאורך הגל של הלייזר, אלא גם לעוצמת השדה ולפרופיל הזמני של הלייזר. מחקרים באטומים ומולקולות נייטרלים וטעונים חיובית הראו כי בתחום השדה החזק החשיבות של אינטראקציות לא לינאריות עולה עם עוצמת השדה, וניתנת לאיפיון לפי מספר הפוטונים המעורבים בתהליך. בעוצמות מספיק גבוהות, כאשר השדה החשמלי שמשרה האור דומה ואף חזק מהכוחות הקושרים את האלקטרונים לגרעינים, שדה הלייזר יכול להיחשב כשדה חשמלי מתנדנד. בתחום זה, מתאים יותר להסתכל על תהליך יינון כמנהור של האלקטרון, ותופעות כגון recollision של האלקטרון הופכות להיות משמעותיות, מה שמוביל לתצפיות של יינון כפול, פליטה קרינתית של תדרים גבוהים (HHG) ופיצוץ קולומבי.

למרות שמחקרים רבים עסקו באינטראקציות הלא-לינאריות של פולסי לייזר עוצמתיים עם מערכות ניטראליות וקטיוניות, כמעט אין בנמצא עבודות העוסקות במערכות מולקולריות אניוניות שמטבען הן שונות. מדידות ניסיוניות חדשות של photo-detachment של אלקטרון בודד, ולאחריו של אלקטרונים נוספים, במערכת האניונית של SF_6^- מולקולרי באמצעות פולסי לייזר קצרים ועוצמתיים, מכוונים להבנת תפקידו של האלקטרון העודף בתהליכים אלו.

מדידות המבוססות על זמן הגעתם של תוצרי האינטראקציה נעשות באמצעות מערכת האצה ייעודית תחת ואקום, ומפאשרות זיהוי של התוצרים השונים. ייעילות היווצרותם של תוצרי האינטראקציה השונים, של תלישת אלקטרון אחד או של אלקטרונים רבים, נבחנת בתלות בפרמטרים שונים של פולסי הלייזר, כגון עוצמה, צורה וקיטוב, וההשלכות על המנגנון של התהליכים נידון. באופן מפתיע אנו מוצאים תלות חלשה של התוצרים בעוצמת הלייזר, וגם קיטוב אליפטי של הפולסים לא מנחית את יעילות היווצרותם של תוצרי multi-detachment כפי שהיינו מצפים ממנגנון המבוסס על recollision. מצד שני, צורת הפולס מגלה השפעה משמעותית על התהליך, בפרט עיוות פאזה על ידי הוספת TOD, שבערכיו השליליים מדכא באופן משמעותי את היינון המגיע לאחר השלב הראשון של נייטרליזציה של ה-SF_6^-. אנו מסיקים כי התהליך האנרגטי של תלישת אלקטרונים נוספים מעבר לאלקטרון הראשון לא מבוסס בעיקרו על מנגנון recollision, אך שלאלקטרון העודף במולקולה האניונית תפקיד חשוב בתהליך היינון שנמשך לאחר תלישתו. תפקידו של האלקטרון העודף נידון בהקשר לאופיו הייחודי של אניון ה-SF_6^-.